

AD-A280 648



Cooling of the West Spitzbergen Current:
Wintertime Observations West of Svalbard

S DTIC
ELECTE
JUN 27 1994
F **D**

TIMOTHY J. BOYD AND ERIC A. D'ASARO*

*Applied Physics Laboratory, College of Ocean and Fishery Sciences,
University of Washington, Seattle, WA 98105*

August 30, 1993

This document has been approved
for public release and sale; its
distribution is unlimited.

DTIC QUALITY INSPECTED 2

*To whom correspondence should be addressed

94-19134



94 6 22 074

NOV 17 1993

ABSTRACT

The West Spitzbergen Current (WSC) is the major source of heat and salt for the Arctic Ocean and the areas of deep convection in the Greenland Sea. The WSC current cools dramatically downstream. Hydrographic and velocity data from a 3-week, midwinter cruise off Spitzbergen are used to investigate the heat budget of the WSC and the mechanisms of cooling. The downstream divergence of mean heat flux in the WSC produces a heat loss of at least $1000 \pm 400 \text{ W m}^{-2}$ averaged over the width of the current. Approximately 350 W m^{-2} is lost to the atmosphere and 200 W m^{-2} is lost to melting ice over a region somewhat wider than the current. Cooling of the WSC to the atmosphere converts the inflowing Atlantic Water (AW) to Lower Arctic Intermediate Water, which is sufficiently salty to convect. Cooling by ice converts the AW to much fresher Arctic Surface Water, which is too light to convect. The relative importance of these two conversions is primarily controlled by the rate at which the wind advects ice from the Barents Sea over the WSC. The warmest water of the WSC is often observed 100–200 m below the surface. Despite the lack of direct contact with the surface, this warm core cools at about 800 W m^{-2} in our observations. This rate is too large to be caused by diapycnal diffusion. We suggest that the energetic eddy field in this area diffuses heat along the steeply sloping isopycnal surfaces that connect the warm core to the surface, renewing the surface layer several times per day. This is consistent with the very shallow surface mixed layers and high level of intrusions observed. We conclude

that the surface layer of the WSC is cooled by the atmosphere and by ice from the Barents Sea, and that isopycnal diffusion by mesoscale eddies continually renews this surface, thus cooling the interior of the WSC. The relative magnitude of these processes determines whether the inflowing warm, salty AW is converted to light, fresh surface water or salty, cold intermediate water.

Accession For	
NTIS CRA&I	<input checked="" type="checkbox"/>
DTIC TAB	<input type="checkbox"/>
Unannounced	<input type="checkbox"/>
Justification	
By	
Distribution /	
Availability Codes	
Dist	Avail and/or Special
A-1	

1. INTRODUCTION

Fram Strait, between Greenland and Svalbard, is the site of most of the exchange of mass, heat, and salt between the Arctic Ocean and the rest of the world's oceans. Atlantic Water (AW) carried northward along the eastern side of the Greenland Sea by the West Spitzbergen Current (WSC) is well known as the major source of heat and salt for the waters of the Arctic basins. Approximately $5-8 \times 10^6 \text{ m}^3 \text{ s}^{-1}$ [Hanzlick, 1983; Aagaard and Greisman, 1975] of the AW in the WSC flows northward through Fram Strait and enters the Arctic Ocean with temperatures up to 3.5°C and salinity of 35 psu. The East Greenland Current (EGC) transports colder, fresher ($T \approx -1^\circ$, $S < 34.4$ psu, Hopkins [1991]) water southward through the western part of Fram Strait. Between these two currents lies the weakly stratified Greenland Sea. Here, salty water from the WSC cools and is modified by mixing with other water masses [Aagaard and Carmack, 1989] and ice. Intermittently, it becomes dense enough to convect to great depth, thus forming a variety of salty (≈ 34.9 psu), cold ($< 0^\circ\text{C}$), deep, and intermediate waters [Swift and Aagaard, 1981; Aagaard et al., 1985]. These overflow the passages between Greenland and Europe and are a major source of deep water for the world ocean.

The WSC cools rapidly as it flows northward toward and into Fram Strait. Climatological wintertime temperatures near Bear Island (74.5°N) are about 5°C while those north of Spitzbergen (81°N) are about 2°C [Dietrich, 1969; Gorshkov, 1983]. This rapid decrease in temperature in the direction of flow indicates a rapid cooling of the current.

A typical temperature gradient of 0.5°C per 100 km over 100 m depth and a typical northward velocity of 0.25 m s^{-1} imply a heat loss of 525 W m^{-2} . This is comparable to the climatological wintertime heat flux from the ocean to the atmosphere in ice-free regions of the WSC, about 400 W m^{-2} [Häkkinen and Cavalieri, 1989]. Our goal is to verify these large wintertime heat losses using velocity and temperature gradient estimates from a synoptic survey.

A classical model [Worthington, 1970] of deep water formation in the Greenland Sea takes (relatively) warm, salty AW from the WSC and subjects it to atmospheric cooling to form cold, salty water dense enough to convect. Aagaard and Carmack [1989], among others, observe that if the warm AW contacts ice, either from the transpolar drift [Untersteiner, 1988] or from the Barents Sea [Vinje, 1985], the resulting meltwater will likely reduce its density such that convection cannot occur. A second goal of our work is to understand what controls the relative amounts of ice and atmospheric heat fluxes in cooling the WSC.

Off northern Spitzbergen [Aagaard et al., 1987], the warmest waters of the WSC are subsurface, at 100–200 m depth, and separated from the surface by roughly 0.1 kg m^{-3} of stratification. Nevertheless, the warm water continues to cool in the downstream direction at about 200 W m^{-2} . If we model this as vertical diffusion, a diffusion coefficient of about $2 \times 10^{-3}\text{ m}^2\text{ s}^{-1}$ would be required, several orders of magnitude above traditional values [Gregg, 1989]. Our third goal is to understand how the stratified

ocean can sustain such large vertical heat fluxes.

In this paper we describe measurements of the WSC made off Spitzbergen during January and February 1989 (Figure 1) as part of CEAREX, the Coordinated Eastern Arctic Experiment, using the *MV Polarbjorn*, a coastal freighter outfitted for this experiment. We chose the experiment region for its relatively simple bathymetry; the warmest water of the WSC flows northward just inshore of the 1000-m isobath. We chose the region's downstream length large enough for significant cooling to be observed and its width to encompass the warm water of the WSC. We also extended sections east and west from the main experimental area. Much of our CTD data was taken by continuously yo-yo'ing a CTD while slowly steaming (a "tow-yow"), thus allowing us to resolve the very small baroclinic deformation radius, typically 2–10 km. Mostly, we operated in the marginal ice zone. Shifting ice prevented the execution of a simple across/along-stream pattern of transects, and the complicated station pattern shown in Figure 1 resulted.

Fig. 1

Section 2 describes the instruments used and the data processing required to correct for their limitations. Section 3 describes the velocity, temperature, and density structure of the WSC averaged over about 50 km. The heat budget on this scale is explored in section 4. First, the integral of $\mathbf{v} \cdot \nabla T$ estimates the heat loss from the WSC ($600\text{--}1200 \text{ W m}^{-2}$). Next, simple models of ice melt rate and of ice advection provide two complementary estimates of the oceanic heat loss to ice ($\approx 200 \text{ W m}^{-2}$). Finally, meteorological measurements give the heat loss to the atmosphere ($\approx 350 \text{ W m}^{-2}$). Exam-

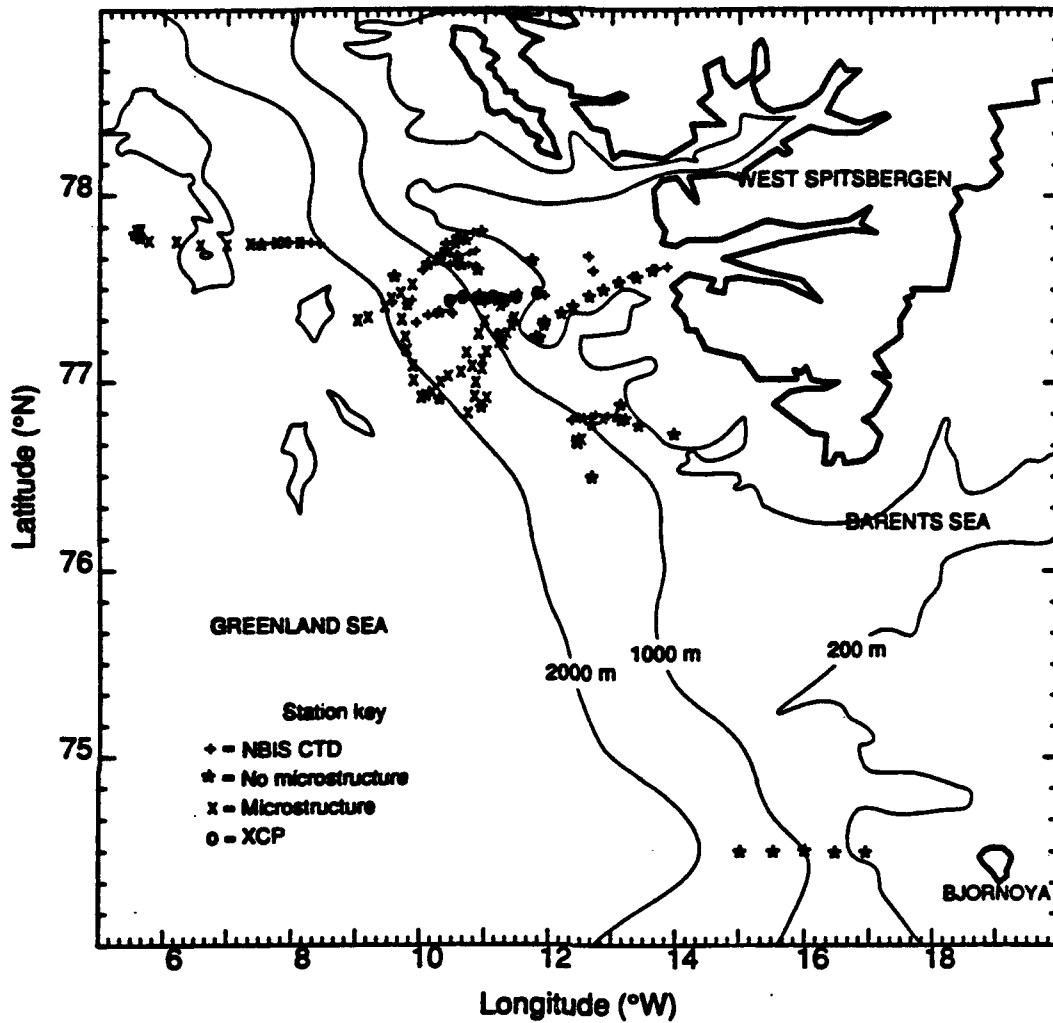


Fig. 1. Map of operating area. Measurements were made along a nearly straight section of the continental shelf and slope west of Spitzbergen.

ination of T/S properties in section 5 shows that cooling by ice produces a very different mass than cooling by air. A simple model rationalizes the T/S slope of the ice-cooled Arctic Surface Water. Section 6 examines the depth and variability of the upper mixed layer. The combination of high winds and rapid cooling imply very rapid mixed layer growth, an average mixed layer age of less than a day, and a rapid exchange of water between the cooled surface and the cooling interior. Mechanisms for this exchange are evaluated in section 7. Outrageously large diapycnal turbulent mixing would be required to produce the required exchange, whereas it is easily accomplished by eddy mixing along outcropping isopycnals. These results are summarized in section 8. The implications for deep and halocline water formation are discussed in section 9.

Many of the calculations, although simple in principle, are complex in detail. We have tried to separate the details from the essence in each section, and encourage the more casual reader to skip the details on a first reading.

2. INSTRUMENTS

2.1. CTD Data

Instruments. We used three different CTDs, each in a different way. In heavy ice and for bottle casts, we used a Neil Brown Mark IV (NBIS) CTD. The winch was located in the ship's hold, and the CTD was stored in a heated hut on the deck between casts. A small region of open water between the ship's hull and the ice could usually be maintained for the CTD casts. This instrument provided most of the data inshore of the shelf break, where the ice was heaviest.

Closely spaced sections of CTD data were obtained using two unpumped Sea-Bird SBE-19 internally recording CTDs incorporated into stably falling frames. These were deployed from the covered fantail with the ship under way at $1-1.5 \text{ m s}^{-1}$ and retrieved with a light line and a winch. Casts were typically to 200 m, with a separation between profiles of 2 km and a duration of up to 3 hours. In open water or very thin ice, we used a slowly falling frame (about 0.5 m s^{-1}) for both CTD and microstructure measurements with the SBE-19s. In moderate ice, we used a heavily weighted frame (falling $1.5-2 \text{ m s}^{-1}$), which we deployed in the small wedge of ice-free water behind the ship. The combination of unexpectedly heavy ice and a very light line made retrieval exciting at times, but neither profiler was lost.

Calibration. Two-liter Niskin bottles mounted on a 12-position General Oceanics rosette were used to take water samples on each NBIS CTD station. Bottles were removed from the rosette and taken inside before samples were drawn. Salinity was measured on the *Polarbjorn* using a Guildline model 8400 AutoSal. Replicate samples were taken throughout the cruise, and their salinity was determined at the University of Washington after the cruise, also using a Guildline model 8400. Replicate bottles had an average difference of 0.004 psu and a standard deviation of 0.004 psu.

Seven intercomparison casts were made with one or both SBE-19 CTDs attached to the NBIS CTD. With the bottles from these casts and the post-cruise calibrations, the SBE-19 salinities differed from the 26 bottle salinities by 0.003 psu on average with a standard deviation of 0.006 psu. The uncorrected NBIS salinities differed from the bottles and calibrated SBE-19s by an average of 0.213 psu with a standard deviation of 0.016 psu. The NBIS CTD's pressure was 0.03 MPa low, and its temperature was 0.027°C low. Its conductivity, temperature, and pressure were therefore offset to match that of the SBE-19s and bottles.

Processing. The NBIS CTD was processed as described by O'Hara [Eastern Arctic Ice, Ocean, Snow and Atmospheric Data, Vol. 1, on CD-ROM, National Snow and Ice Data Center, University of Colorado, Boulder, 1992], subsampled to 10-kPa (1-dbar) intervals for use here.

The Sea-Bird CTDs were not pumped and therefore required several corrections. The difference in response time between the temperature and conductivity sensors produces salinity "spikes" a few meters thick in high gradient regions. Lagging the conductivity relative to temperature and pressure by T_{lag} minimizes these spikes. Since the salinity sensors were not pumped, T_{lag} depends on fall rate. We found that a T_{lag} varying from 0.46 s at a fall rate of 0.25 m s^{-1} , to -0.29 s at a fall rate of 1 m s^{-1} , and to -0.26 s at a fall rate of 2 m s^{-1} minimized the spiking.

The thermal inertia of the SBE conductivity cells [Lueck and Picklo, 1990; Lueck, 1990] causes significant errors in density which decay on time scales of tens of seconds. Lueck and Picklo [1990] model this effect in terms of two parameters: the magnitude of the conductivity error is proportional to α ; it decays at a rate β . Their data were taken at a higher fall rate than any of our profiles, and we found that their parameter values did not properly correct our data. We therefore derived our own, fall-rate dependent values, obtained by minimizing the number and intensity of density inversions in groups of profiles with similar fall rates. The following expressions fit both our estimates and Lueck and Picklo's to within 5%.

$$\alpha = (-0.10443 \log_{10}(|W|) + 0.138564) \frac{0.5}{|W|} \quad (1a)$$

$$\beta = 0.046962 \log_{10}(|W|) + 0.085137 \quad [\text{s}^{-1}] \quad (1b)$$

where $|W|$ is the fall speed in meters per second. The value of α varies from 0.38 at our slowest fall speed (0.4 m s^{-1}) to 0.018 at Lueck and Picklo's fall speed (2.5 m s^{-1}). The

thermal correction to the conductivity is thus largest at the smallest fall rate. The decay time β^{-1} varies less, from about 16 s at 0.4 m s^{-1} to about 10 s at 2.5 m s^{-1} . Further discussion and comparison with other data are provided by *Morison et al.* [1993].

We correct the SBE-19 data for both spiking and thermal inertia, obtaining independent estimates of salinity and density every 18 m. The conductivity cell takes about 50 m to thermally equilibrate after the CTD enters the water, so only the tow-yo profiles provide near-surface density data. Temperature, with a resolution of 1 m, is unaffected by these corrections. With this processing, the fraction of data with density inversions is reduced from 17% to 6.7%, the average magnitude of inversions is reduced from 0.001 kg m^{-3} to $0.00013 \text{ kg m}^{-3}$, and the average maximum density in each inversion is reduced from 0.002 kg m^{-3} to 0.0007 kg m^{-3} . The coefficients proposed by Lueck and Picklo are approximately half as effective as (1). An example of the improvement in a single profile can be seen in Figure 2.

Fig. 2

2.2. XCP Velocities

Profiles of horizontal velocity along a single section (Figure 1) at 77.4°N were made on January 26 using 10 Expendable Current Profilers (XCPs) manufactured by Sippican [*Sanford et al.*, 1982]. Nine of these yielded high quality data. Data were collected using a Sippican MK-10 deck box as described by *D'Asaro et al.* [1990]. The processing is described by *D'Asaro and Morison* [1992]. The XCP yields estimates of horizontal velocity relative to an unknown, vertically uniform offset. A velocity sample is

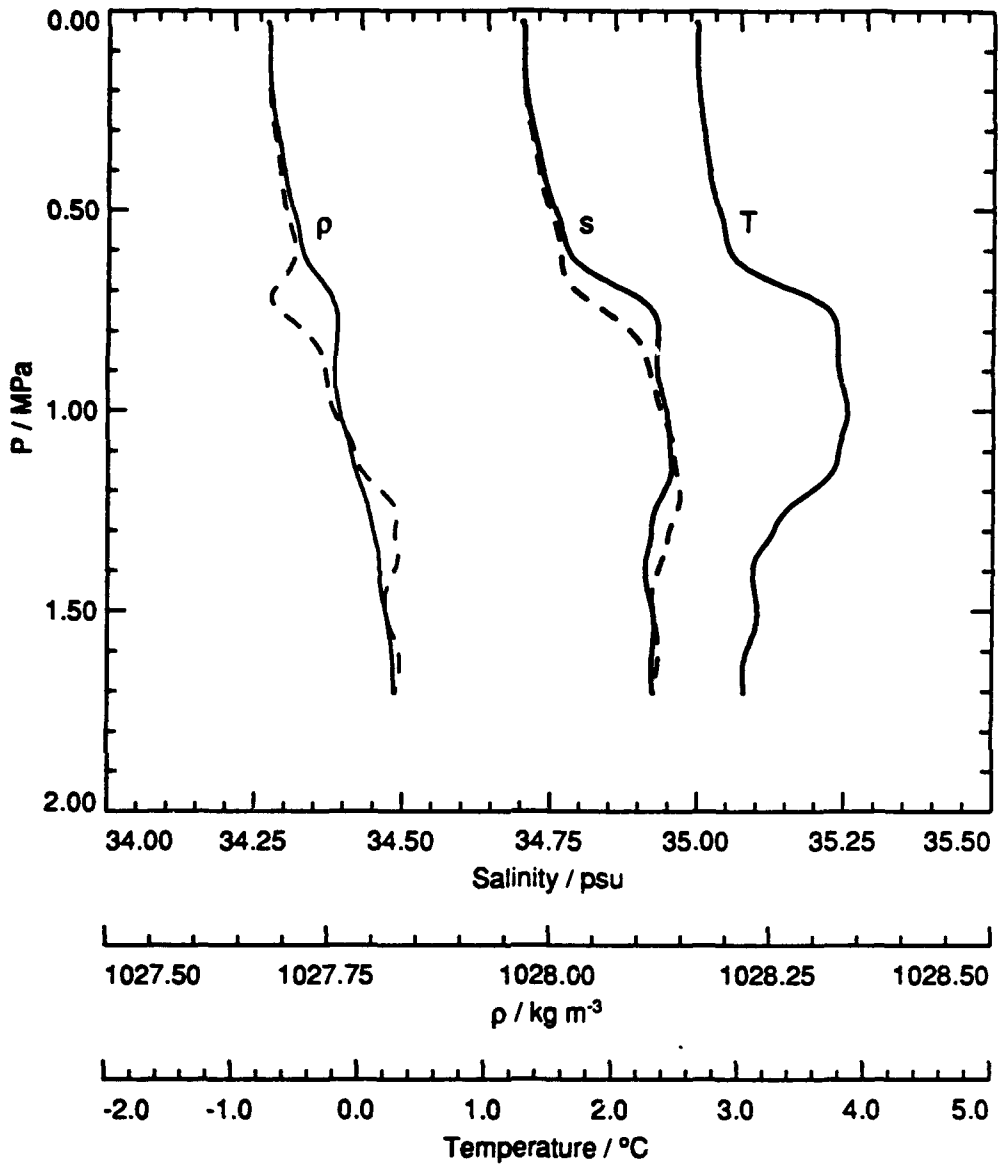


Fig. 2. Example of CTD processing. Dashed profile is uncorrected data. Solid profile is data with thermal lag correction applied. The correction removes density inversions associated with rapid temperature changes (1 MPa = 100 dbars).

obtained every 0.3 m. Averaging these in 10-m bins gives velocity errors of about 0.008 m s^{-1} .

2.3. *Meteorology*

Wind and air temperature measurements were made on the *Polarbjorn* 10–18 times per day by a NOAA meteorological observer and the bridge officers, using the ship's anemometer and thermometer and visual estimates of the wind direction.

2.4. *Near-Surface Velocity*

Instruments. Near-surface currents relative to the ship were measured using a 150-kHz RDI Acoustic Doppler Current Profiler and a single-axis hull mounted Sagem LH electromagnetic log. The ADCP was damaged by ice on a previous leg of CEAREX and provided no useful data. A robust estimate of the water velocity was obtained by combining data from the electromagnetic log, GPS navigation, and ship's orientation from the gyrocompass. Each of these instruments provided poor data at times, so a complex editing procedure was necessary.

Processing. We do not know the absolute accuracy of the electromagnetic log, but it produced consistent answers. At low speeds, we expect a large velocity component transverse to the ship. We therefore discarded speeds less than 0.5 m s^{-1} . The remaining data were averaged with a 160-second-wide boxcar window.

A Magnavox 1107-GPS with atomic clock measured the position and velocity of the ship. Two satellites, required to provide a fix, were available during 62% of the cruise. The manufacturer claims a position fix accuracy of 15 m rms and a velocity accuracy of 0.05 m s^{-1} after filtering the raw GPS data with the built-in Kalman filter. The data clearly contain errors much larger than this, which we removed by careful editing. Data were flagged "bad" if a change in satellite constellation had occurred within the past 3 minutes, if the 160-second, boxcar filtered acceleration had been greater than 1 m s^{-1} per minute within the past 6 minutes, or if the Dilution of Precision had been greater than 50 within the past 2 minutes.

The ship's gyrocompass (Anschutz std. 4) provided heading data. The measured heading was corrected for the difference between dynamic and geographical north [Christou, 1983] caused by the northward velocity of the ship, estimated from the GPS data. At these latitudes, gyrocompasses may have large errors; they generally become useless above about 80°N [Christou, 1983]. These errors are largest after rapid angular motion, so the heading data were flagged bad if the heading changed by more than 1.2° per second. We usually kept the ship's speed low ($1\text{--}2 \text{ m s}^{-1}$) so that the effect of gyro error on velocity was minimized.

After the above editing, the data were passed through an 1800-s-wide boxcar filter. Data were output every 900 s if the past 1350 s of data had been good. The resulting surface current vectors are not completely independent, but more than every other vector is

independent because of the heavy editing. We obtained good velocity data during only 16% of the experiment.

Alignment and windage errors. The electromagnetic log combined with the gyrocompass yields an estimate of the ship's velocity relative to the water \mathbf{u}_m (measured). Errors in this estimate are caused by alignment errors in the gyrocompass and the log, and motion of the ship due to wind. In addition, the true velocity of the near-surface water is correlated with the wind, as in the well-known Ekman layer. We represent horizontal vector velocities as complex numbers and model the ship's velocity relative to the part of the surface flow that is not wind driven:

$$\mathbf{u}_s = Ae^{i\theta}\mathbf{u}_m + Be^{i\phi}\mathbf{u}_a \quad (2)$$

where \mathbf{u}_s is the ship's velocity and \mathbf{u}_a is the measured wind velocity. The first term on the right accounts for alignment and gain errors in the electromagnetic speed log and gyro, and the second term accounts for both windage on the ship and surface currents correlated with the wind. We model the water velocity \mathbf{u}_w as the difference between the GPS-measured ship velocity relative to the ground \mathbf{u}_g and \mathbf{u}_s ; $\mathbf{u}_w = \mathbf{u}_g - \mathbf{u}_s$. We require that \mathbf{u}_w be uncorrelated with both the wind and the ship's motion.

$$\begin{aligned} \overline{\mathbf{u}_w \mathbf{u}_m^*} &= 0 \\ \overline{\mathbf{u}_w \mathbf{u}_a^*} &= 0 \end{aligned} \quad (3)$$

where the overbar denotes the along-track average, and the correlation excludes periods with wind speed greater than 40 knots. This yields

$$\mathbf{u}_s = 0.92e^{i(0.5^\circ)}\mathbf{u}_m + 0.01e^{i(-28^\circ)}\mathbf{u}_a \quad (4)$$

where positive angles are counterclockwise. The wind induces a velocity component to the right of the wind at about 1% of the wind speed, qualitatively consistent with an Ekman layer. In addition, the small gain and angle corrections in the first term imply that the speed log and gyro do not have large errors.

2.5. Ice Data

Estimates of ice concentration, P_{ip} , were made visually from the *Polarbjorn*. They were intermittent, made in low light, largely by untrained observers (including the authors), and are biased toward low ice, warm water conditions where CTD operations were possible. Daily maps of ice concentration from SSM/I satellite measurements, P_{is} , were obtained from the National Snow and Ice Data Center, University of Colorado. These cover the experimental area in all weather, but with a spatial resolution of only about 50 km. In the marginal ice zone the errors are about 10% (Don Thomas, personal communication). The P_{ip} are correlated with the P_{is} interpolated to the same time and location with $r = 0.67$. Only the P_{is} have the necessary space and time coverage, and we will use them here.

3. STRUCTURE OF THE WSC

3.1. *Coordinates*

We define an along-stream (y) and cross-stream (x) coordinate system with its origin at the intersection of 77.4°N and the 1000-m isobath. All geographic data will be presented in this system. We divide the data into five "sections" across the WSC: one west of Bjornoya at $y = -375$ km, and the remaining four in the intensively sampled region between $y = -100$ km and $y = 50$ km. The sections generally contain data taken during one day. Sections $y = 0$ km and $y = 25$ km contain some "nonsynoptic" data on their eastern end which extend them onto the shelf. Table 1 lists the times and locations of each section.

Table 1

3.2. *The Warm Core*

Figure 3 displays the temperature at 150 m depth. A circle gives the location of each CTD profile; its color indicates the temperature. Colored contours show the smoothed 150-m temperature, generated by objective mapping of the data [Bretherton *et al.*, 1976] with a cross-stream Gaussian decorrelation scale of 40 km and an along-stream scale of 80 km north of -50 km and 320 km south of -50 km. The variable along-stream correlation scale allows the Bjornoya section ($y = -375$ km) to be included in the analysis. Contours are not drawn where the error in the mapped temperature exceeds 30%. By comparing the colored circles and the contours, it is clear that the data resolve the large scale structure of the WSC and that smaller scale, unresolved temperature features ("eddies") also exist.

Fig. 3

TABLE 1. Downstream Coordinate and Time Limits for the Sections

y_{nominal}	$y_{\text{min}}, \text{ km}$	$y_{\text{max}}, \text{ km}$	day_{min}	day_{max}
-375	-367.8	-357.2	16.1	16.6
-75	-95.0	-82.8	21.5	21.9
-25	-33.0	-17.2	28.0	29.6
0	-9.7	4.8	25.8 29.8	27.0 31.1
25	22.4	35.6	20.0	23.0

Day 1.5 is 12 noon on January 1, 1989.

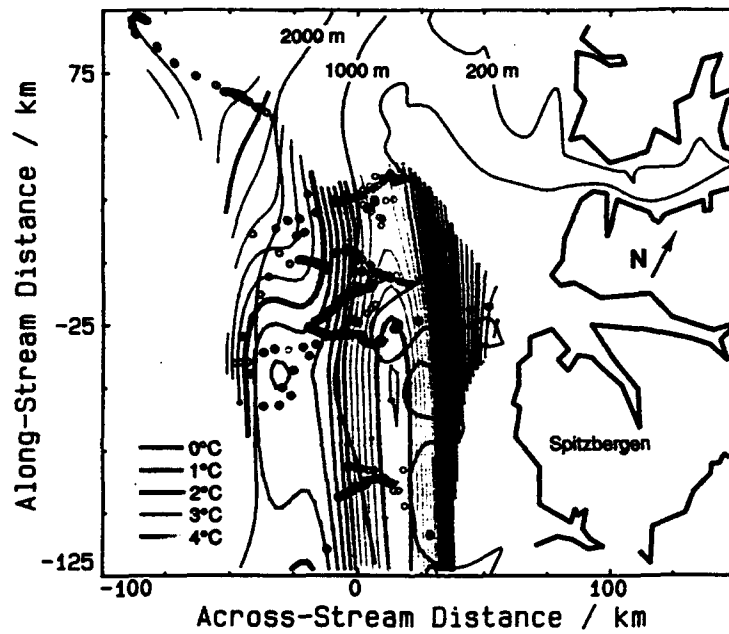


Fig. 3. Map of potential temperature at 150 m depth from all CTD data. Colored symbols show the location of data points; the color indicates the temperature as given on the scale. Colored contours display an objective mapping of the temperature. Temperatures greater than 4°C are shaded red. The warm core of the West Spitzbergen Current is apparent.

A ribbon of warm water, just inside the 1000-m isobath, dominates the temperature at 150 m. We call this the "warm core" of the WSC. Colder water lies to the east on the Spitzbergen shelf and to the west in the Greenland Sea. As anticipated, the maximum temperature of the warm core decreases northward, suggesting rapid cooling.

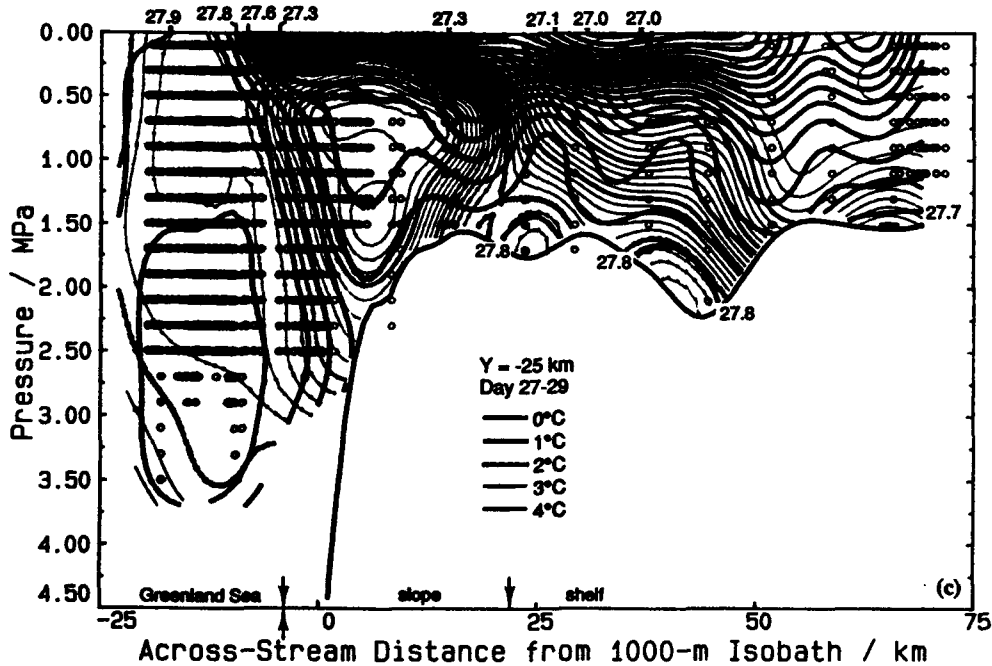
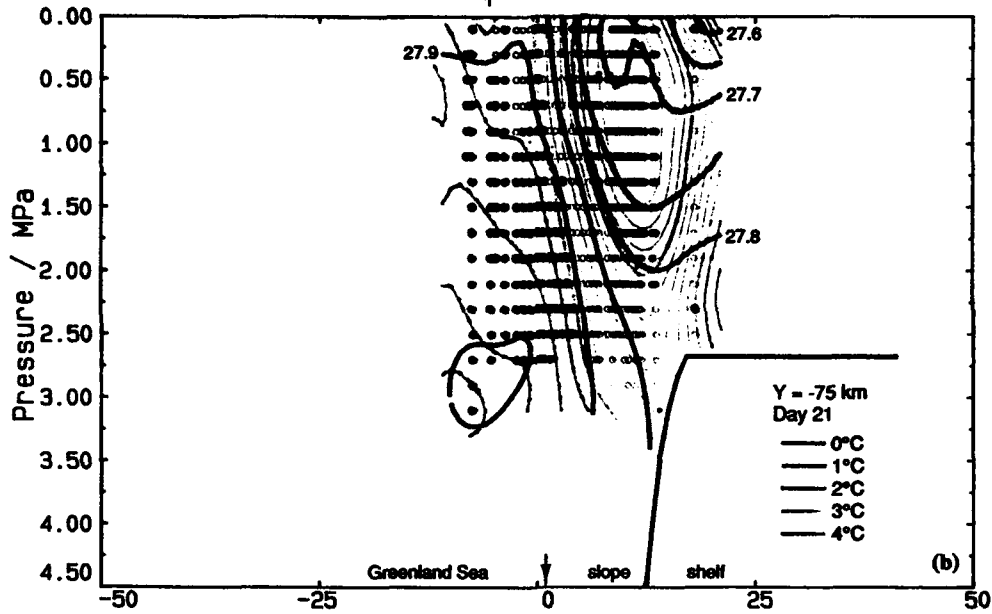
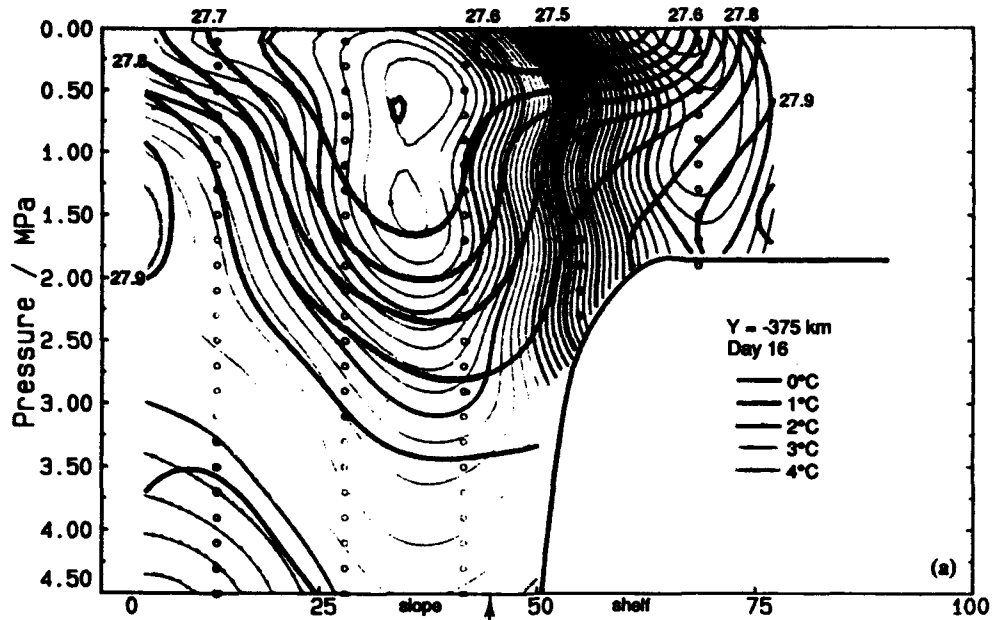
3.3 Hydrographic Sections

Five sections across the WSC (Figures 4a–4e) show individual CTD data points as colored circles, the color denoting the temperature; temperature contours are colored and density contours are black. Objective analysis using a vertical correlation scale of 75 m produced the contoured fields. An across-stream correlation scale of 8 km was used at all sections except the Bjornoya section, where 20 km was used. Figures 1 and 3 show the geographical location of the data.

Fig. 4

The warm core, centered over the slope in each section, reaches almost to the surface in the south, Figures 4a and 4b, but descends to 100–150 m in the north, Figures 4c–4e. It cools from a maximum temperature of about 5.5°C in the south (Figure 4a, $y = -375$ km) to 4.4°C at the northern end (Figure 4e, $y = 25$ km).

In each section, isopycnals passing through the warm core of the WSC ($\sigma_\theta \approx 27.75$) outcrop to the surface near the offshore edge of the warm core to form a surface density front. This front separates the stratified warm core of the WSC from the cold, weakly stratified water of the Greenland Sea. Note the stations with almost homogeneous water



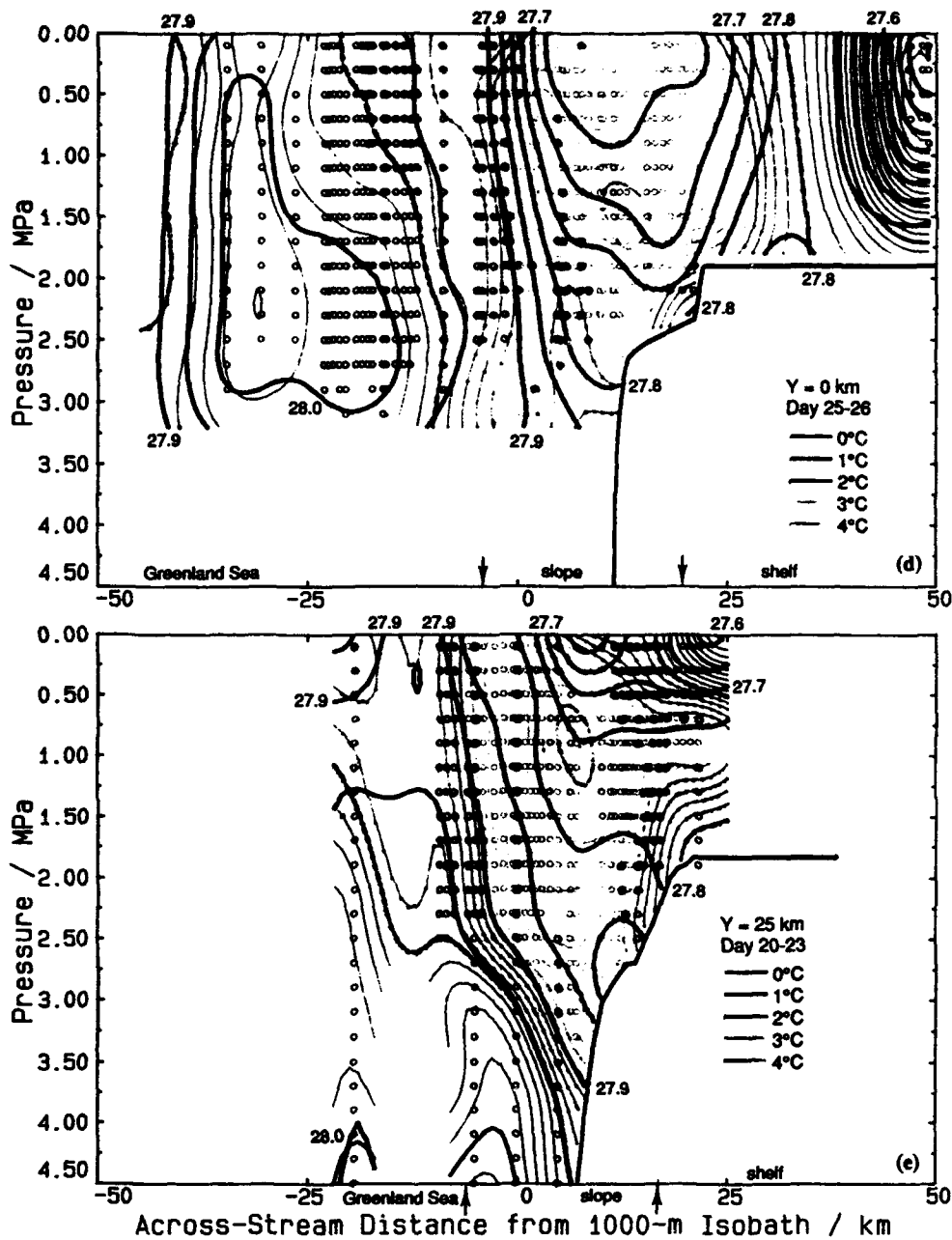


Fig. 4. Potential temperature and density sections. Colored symbols show the location of data points; the color indicates the temperature as given on the scale. Colored contours display an objective mapping of the temperature. Temperatures greater than 4°C are shaded red. The temperature contour interval is 0.2°C. Dark contours indicate the same objective mapping of σ_θ . The density contour interval is 0.05 kg m⁻³. First section (a) is at Bjornoya. The data locations for Figures 4b–4e are shown in Figure 3, and the approximate downstream location is given on each map. The warm core of the West Spitzbergen Current is apparent over the slope in each section.

to 250 m in the Greenland Sea ($y = 0$ km, Figure 4d). Inshore of the warm core, on the Spitzbergen shelf ($y = -25$ km, Figure 4c), the stratification increases with cold, fresh water overlying warmer, saltier water, perhaps owing to the inshore intrusion of warm WSC water along the bottom.

3.4. *Horizontal Structure of Velocity*

Near-surface velocity vectors computed from the electromagnetic log, GPS navigation, and the ship's gyrocompass (Section 2) show flow generally along bathymetry and northward (Figure 5). Near $y = 0$ km, the vectors suggest an eddy. The 150-m temperature also shows an anomaly here (Figure 3). We divide the data into shelf, slope, and Greenland Sea regions, as indicated in Figure 5, further subdividing the slope region into north, south, and eddy regions. For each region, we compute the average downstream and cross stream velocities (Figure 6). Except for the northern slope, the downstream velocity differs little between regions. We characterize the entire region by a single average downstream velocity, $\bar{v} = 0.35 \pm 0.09 \text{ m s}^{-1}$. The average cross-stream velocity, $\bar{u} = 0.05 \pm 0.06 \text{ m s}^{-1}$, is not significantly different from zero (error ranges are one standard deviation). The data indicate a small convergence of water from the Greenland Sea and shelf onto the slope, which also is statistically insignificant. Since these velocities do not include wind-forced motions (the wind-related component (3) averaging 0.06 m s^{-1} directed toward 335°T having been removed), they estimate the surface geostrophic velocities.

Fig. 5

Fig. 6

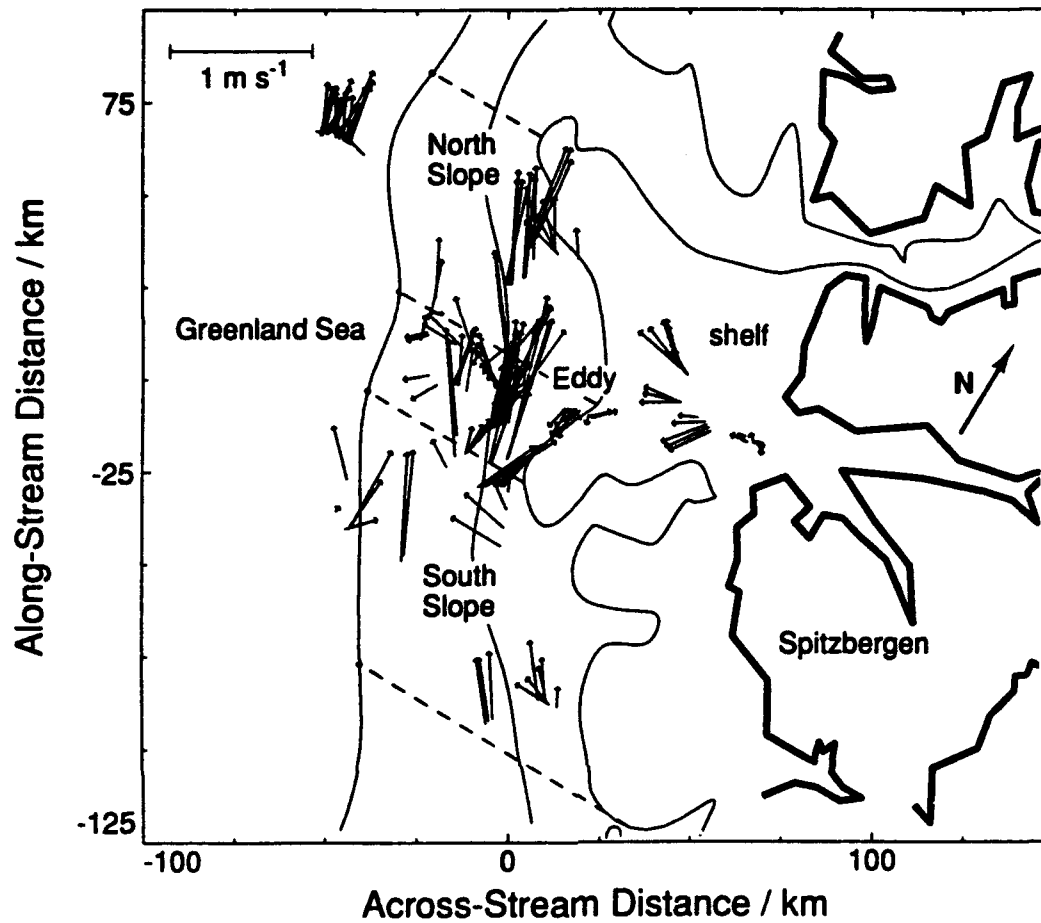


Fig. 5. Near-surface velocity vectors computed from ship's speed log and gyrocompass heading and GPS navigation. Careful editing has resulted in this small set of vectors. Geographical regions defined by the depth contours and the dotted lines are labeled. The water flows northward along the slope.

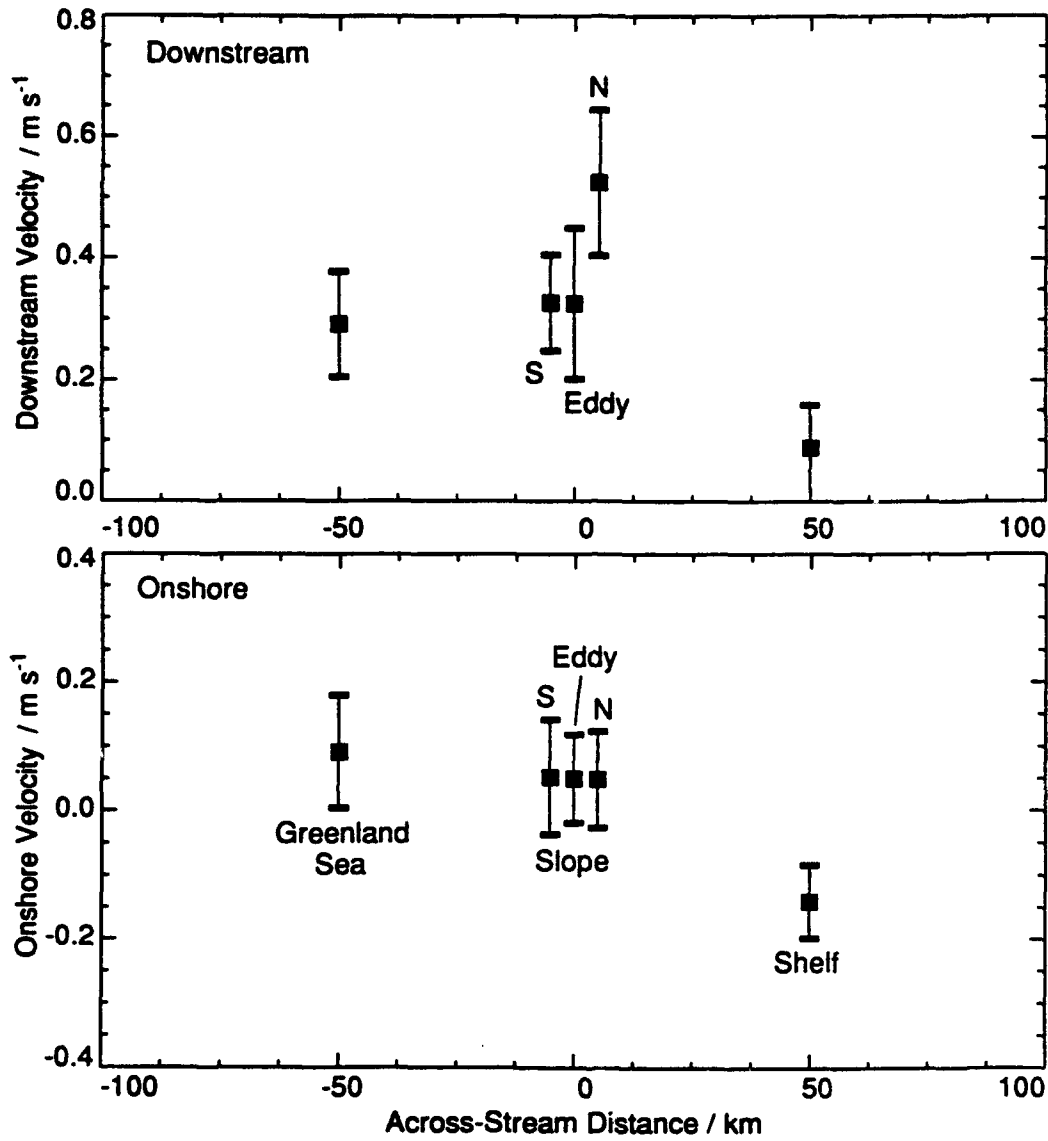


Fig. 6. Average downstream and onshore surface velocity in each of the regions defined in Figure 5. Error bars are one standard deviation.

3.5. Vertical Structure of Velocity

Although the XCP section provides accurate measurements of the baroclinic velocity along one section, a complete velocity section also requires an estimate of the barotropic component for each XCP profile. All of our XCPs profiled the bottom boundary layer. Four of them showed clear logarithmic boundary layers extending from the bottommost sample at 0.6 m above the bottom to about 20 m above the bottom. *Jones and Sanford* [1989] and *Sanford* [1986] show many other examples of this and discuss the estimation of bottom drag from similar data. We use the near-bottom shear to infer the direction of the bottom velocity.

We estimate the downstream barotropic velocity for each XCP profile as an optimization problem. First, we minimize the rms horizontal shear, since the surface velocity (Figure 5) shows little horizontal shear. Then we simultaneously minimize the rms bottom velocity, since the XCPs with zero bottom velocity predict surface velocities close to those in Figure 6. Finally, we require that the bottom velocity have the same sign as the near-bottom XCP shear, except over the shelf where the bottom current was set to zero. We objectively map the resulting downstream velocity as in Figure 4 and display it in Figure 7.

Fig. 7

The estimated currents increase toward the surface, with a maximum speed of 0.5 m s^{-1} and little variation across the slope. Only weak currents appear on the shelf. The average downstream surface velocity computed from the XCP section over the slope

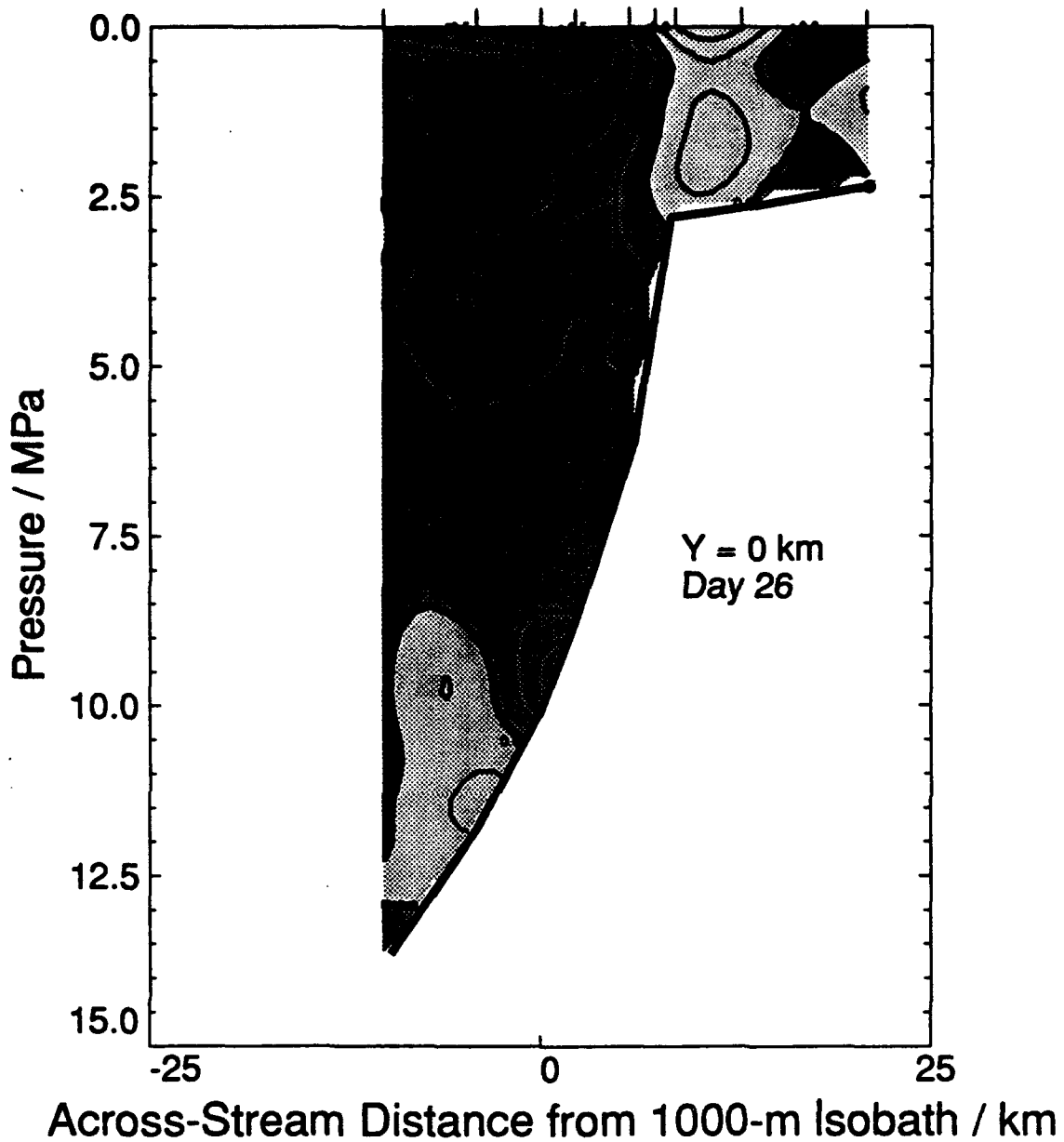


Fig. 7. Section of downstream velocity from XCP data. Contour interval is 0.1 m s^{-1} . The maximum surface velocity is just above 0.5 m s^{-1} . Heavier shading indicates northward flow. Velocity offsets for each XCP profile have been estimated (see text) and the data objectively mapped for plotting here. Note much larger depth axis than in other sections.

(0.45 m s^{-1}) is between the electromagnetic log value in the "eddy" region ($0.54 \pm 0.12 \text{ m s}^{-1}$) and that in the "north" region ($0.32 \pm 0.12 \text{ m s}^{-1}$), indicating that our inversion is reasonable. The vertical shear in the downstream velocity component averages 0.14 m s^{-1} per 100 m in the upper 200 m over the slope ($-10 \text{ km} < x < 8 \text{ km}$), about double the geostrophic shear (0.05 m s^{-1} to 0.09 m s^{-1}) computed from the sections (Figure 4). The difference most likely reflects geographical variations. We note that the transport of the XCP section is 2.7 Sv, comparable to *Hanzlick's* [1983] value of 2.0 Sv over about the same region (his region 'C').

4. FLUXES

We write the budget for oceanic heat, q , of our experimental region as

$$\frac{d\bar{q}}{dt} + \bar{v} \cdot \nabla \bar{q} = -\nabla \cdot \overline{v'q'} \quad (5a)$$

where \bar{q} , \bar{v} , and $\overline{v'q'}$ are the average heat content, velocity, and eddy heat flux within the volume. We integrate (5a) and further assume that only the eddy heat fluxes at the surface are important.

$$\frac{d}{dt} \int_{\text{volume}} q \, dx \, dy \, dz = \int_{\text{surface}} (Q+H) \, dx \, dy - \int_{\text{volume}} \bar{v} \cdot \nabla \bar{q} \, dx \, dy \, dz \quad (5b)$$

where the terms represent the surface heat fluxes to air, Q , and to ice, H , and the divergence of the mean heat flux. We now compute and compare the right-hand terms.

4.1. Ocean Heat Flux Divergence

Methods. We assume that the velocity field is uniform (Figure 6) and compute the average heat flux divergence with units of watts per downstream meter as

$$\bar{v} \rho_w c_w \frac{d}{dy} \int \theta dA \quad (6)$$

where c_w and ρ_w are the specific heat and density of seawater, respectively, θ is the field of objectively mapped temperature (Figure 4), and \bar{v} is the average downstream current. For \bar{v} we use the average surface velocity from Figure 7 ($0.35 \pm 0.1 \text{ m s}^{-1}$), corrected for the average difference in geostrophic velocity between the surface and 100 m ($0.060 \pm 0.02 \text{ m s}^{-1}$), to yield $\bar{v} = 0.29 \pm 0.1 \text{ m s}^{-1}$.

We evaluate the integral in (6) on each section in Figure 4. In addition, we use data from an extensive CTD survey of the Yermak Plateau region taken in March and April 1988 [Muench *et al.*, 1992]. These data are far sparser than ours, and we cannot compute the integral (6) directly. Instead, we estimate the appropriate average temperature from their section 'A-A' at about 81°N .

Conservation of mass requires that the area of integration in (6) for each section be equal. The choice of integration areas defines an assumed mean streamtube. We do not know this flow exactly, but make several reasonable choices and show that a large heat flux divergence results in all cases. Figure 8 shows the areas chosen, Table 2 lists various properties of each streamtube, and Figure 9 plots the average temperature and salinity as a function of y .

Fig 8
Fig 9
T2

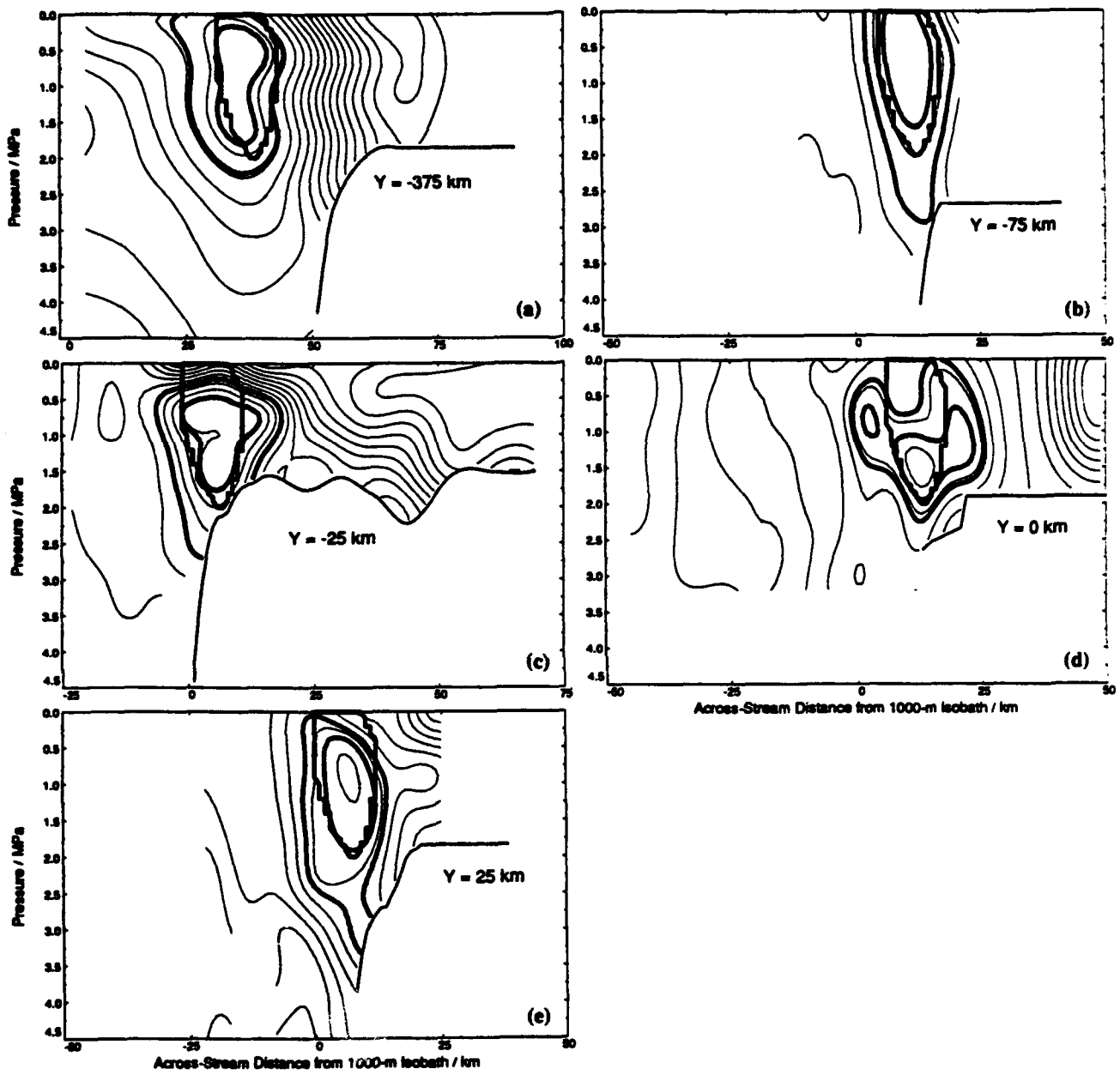


Fig. 8. Streamtube locations in each section. The cross section of each of the three streamtubes is superimposed on the temperature contours from each section. The largest is streamtube 1; the smallest, streamtube 2; and the one with constant shape, streamtube 3.

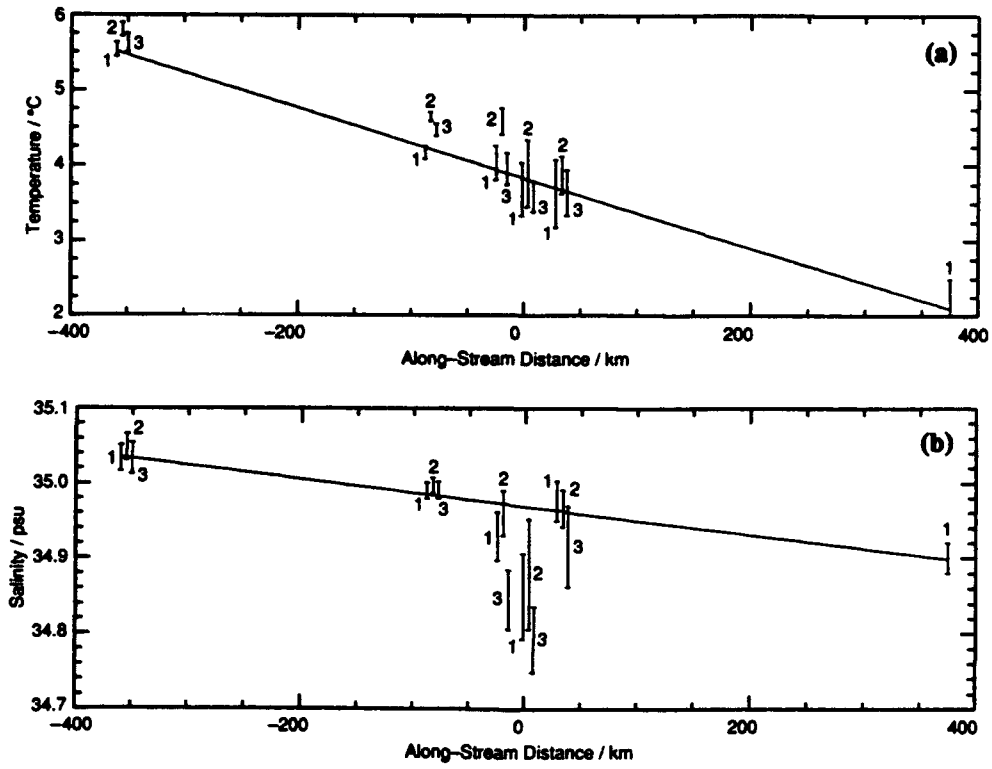


Fig. 9. Average temperature (a) and salinity (b) in each streamtube computed from objectively mapped fields. Errors are one standard deviation of the mean. Solid line is fit of streamtube 1. Table 2 gives other fits. Temperature decreases uniformly to the north. Salinity varies irregularly.

TABLE 2. Oceanic Heat Flux Divergence

Streamtube	$\theta_y,$ $10^{-5} \text{ }^\circ\text{C m}^{-1}$	Divergence,* 10^7 W m^{-1}	Q, W m^{-2}
Main Experimental Area ($\Delta y = 100 \text{ km}$)			
1 (Largest core, 17 km x 209 m)†	-0.41	1.8	1040
2 (Central core, 9.2 km x 130 m)†	-0.51	0.74	800
3 (Constant shape, 12.5 km x 167 m)†	-0.87	2.2	1770
Add Bjornoya Section ($\Delta y = 400 \text{ km}$)			
1	-0.49	2.1	1245
2	-0.43	0.62	680
3	-0.48	1.2	980
Add Yermak Plateau Data ($\Delta y = 750 \text{ km}$)‡			
1	-0.46	2.0	1170
2	-0.47	0.67	740
3	-8.0	20	16200§

*Downstream velocity of 0.29 m s^{-1} assumed.

†Nominal streamtube height times width equals true area; see Figure 8 for actual shapes.

‡ θ estimated visually from *Muench et al.* [1992] figures.

§Streamtube 3 at Yermak Plateau yields obviously wrong results because it is mostly in southward flowing water of East Greenland Current.

First streamtube. Our first choice of streamtube connects the warmest waters in each section. Water cooler than 3.5°C cannot be tracked between sections since such isotherms extend below the data at the $y = -75$ -km section (Figure 4b). We thus define the area of this streamtube by the 3.5°C contour in the -75 -km section and choose the bounding isotherm in the other sections so as to encompass the same area. From south to north these isotherms are 5.1°, 3.5°, 3.0°, 3.4°, and 3.3°.

Second streamtube. The first streamtube extends into the cool surface water in many of the sections. We define a second, smaller streamtube to encompass just the subsurface warm core. It is defined by the 4.5°C contour in the -75 -km section and extended northward in the same manner as the first streamtube.

Third streamtube. The near-surface waters cool dramatically between the southernmost and northern sections. The first two streamtubes descend as they flow northward, thus avoiding this surface region, and implying that the cold surface water advects sideways over the warm core. Alternatively, the cold surface water may be formed by cooling of warm surface water flowing from the south. We choose a third streamtube consistent with this scenario. We defined its fixed shape by the 4.0°C contour in the -75 -km section and center this shape horizontally on the warm core in each section. This streamtube extends into the southward flowing water of the East Greenland Current in the Yermak Plateau section [Muench *et al.*, 1992], which is clearly inappropriate.

Results. For each streamtube we evaluate the average temperature and salinity and its error from the objectively mapped data (Figure 4), or by eye for the Yermak Plateau data. These points are plotted in Figure 9. The northward derivative of temperature and its error are computed from a least squares fit, and the resulting heat fluxes are shown in Table 2.

For all three choices of streamtube, the average temperature decreases downstream (Figure 9a) in both the experimental area ($y = -75$ km to 25 km) and across the extended domain, $y = -375$ km to 375 km. The gradients, $\bar{\theta}_y$, typically about $0.48^\circ\text{C m}^{-1}$ imply enormous heat flux divergences (Table 2), equivalent to a $600\text{--}1200 \text{ W m}^{-2}$ flux from the streamtubes to the surface above (Table 2, last column). The 30% uncertainty in \bar{v} dominates the error in the heat flux divergence, with the error in $\bar{\theta}_y$ contributing only about 6% rms over the extended domain. Using only the main experimental area, the errors in $\bar{\theta}_y$ rise to 20–60% rms. We can probably trust the heat flux divergence estimates to better than a factor of 2.

Streamtubes 1 and 2, centered on the warm core, have nearly the same $\bar{\theta}_y$. Streamtube 1 is larger and therefore has a larger heat loss. Streamtube 3 cools substantially faster within the main experimental area because of an increasing amount of cold surface water to the north, which we will later show is due to ice. Extension of streamtube 3 northward to the Yermak Plateau yields enormous cooling, but this is artificial, since the surface water here is part of the southward flowing East Greenland Current. Unlike tem-

perature, salinity decreases irregularly northward; we will show this is also due to ice.

The heat loss estimates in Table 2 are underestimates because they do not include all of the northward flowing water. For example, almost all the water at the Bjornoya section (Figure 4a) is warmer than 2.5°C, but none of the water at the Yermak Plateau is. All of the water in this section appears to be moving northward, but our streamtubes encompass less than half of it. We cannot, however, make our streamtubes larger and still follow the warm core in a sensible way. It is likely, however, that the total heat loss from the WSC in this region is 50% larger than we estimate, perhaps 3×10^6 W per meter of downstream distance.

4.2. Heat Flux to Ice

The SSM/I-derived ice concentration off Spitzbergen decreases from nearly 100% on the Spitzbergen shelf to 0% offshore of the warm core. (See Figure 10 for examples from the near the beginning and end of our measurements.) We generally found an ice edge much sharper than the approximately 50-km resolution of the SSM/I. The ice concentration also increases with time during our measurements, increasing first in the south (Figure 11a) and then in the north (Figure 11b) and thus suggesting a northward advection of ice.

Fig. 10

Fig. 11

We now compute the average flux of heat from the ocean to the ice over a 50-km by 100-km region centered on the warm core. The 50-km resolution of the SSM/I data

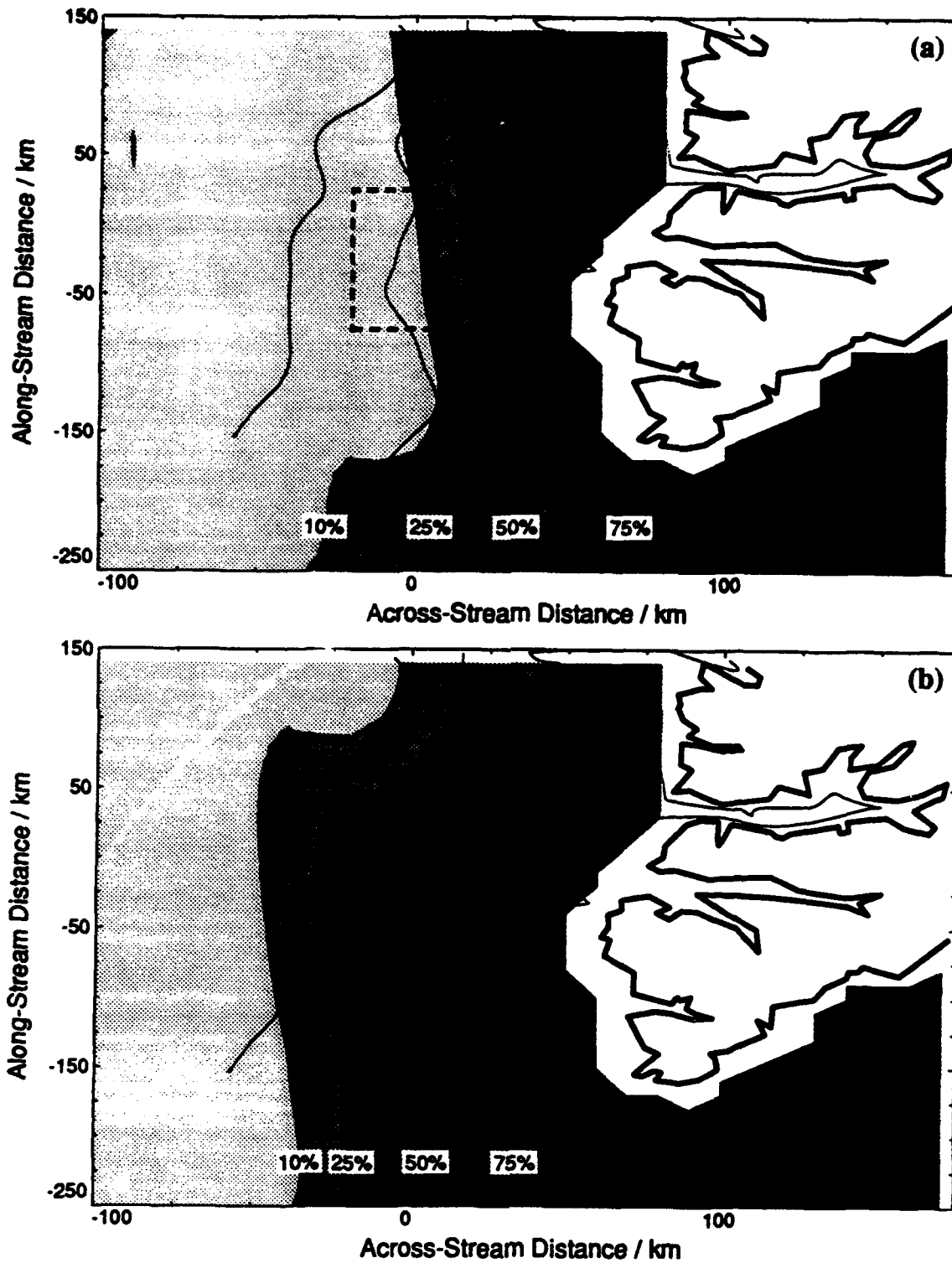


Fig. 10. Ice concentration from SSM/I for (a) day 17 and (b) day 31. The box defines our approximate operating area and the region of heat flux calculations in Figure 12. Note that the ice cover in this region has increased with time.

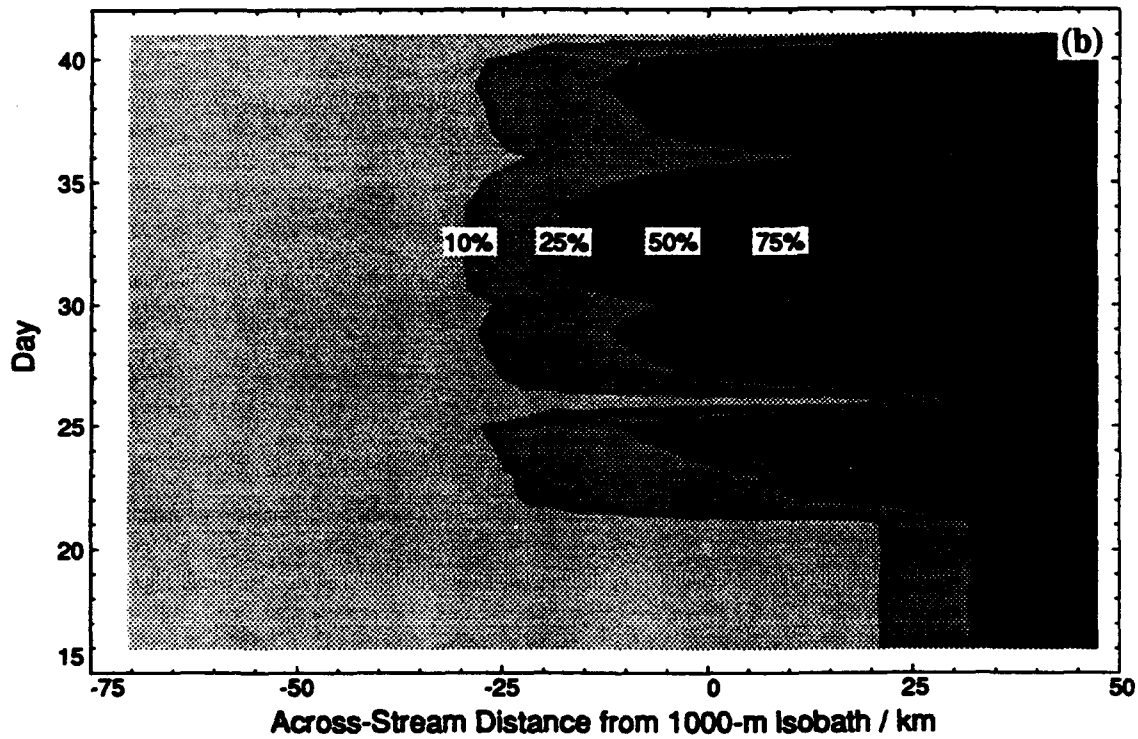
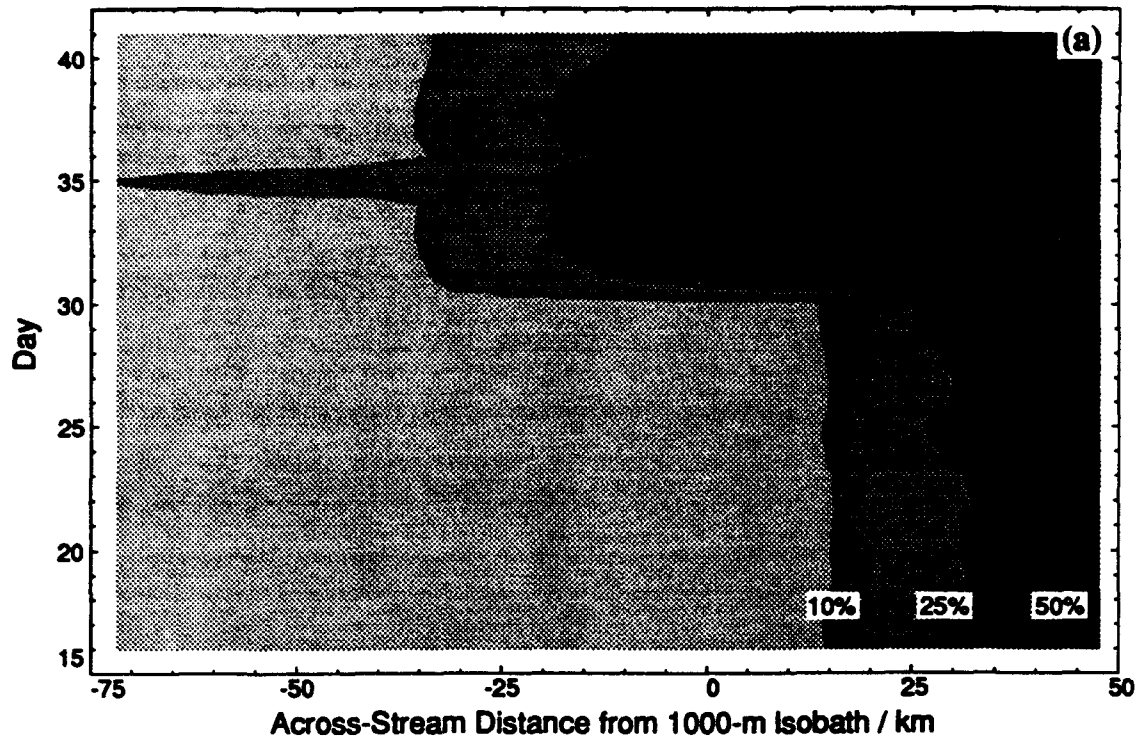


Fig. 11. Ice concentration from SSM/I as a function of time and cross-stream distance at (a) $y = 50$ km and (b) $y = -50$ km. Note that the ice cover increases with time, first in the south and then in the north.

necessarily makes the resolution of this estimate larger than any of our streamtubes. We use *McPhee's* [1987] parameterization generalized for regions of partial ice coverage,

$$H = \rho_w c_w c_H u^* \overline{(T_w - T_f)} P_i, \quad (7)$$

where T_f is the freezing temperature of seawater. Daily SSM/I maps of ice concentration provided estimates of the ice concentration P_i . The thin ice in this region can absorb little momentum (see below) so we equate u^* at the ice-water interface to that at the ice-air interface and estimate both from bulk formulae (see appendix). The water temperature T_w is estimated from P_i since the water was generally warmer in regions of lower ice concentration.

The heat flux to ice (Figure 12d) generally increases with wind speed, owing to the larger u^* , and increases with time, owing to the increasing concentration of ice (Figure 11). The average value of H for days 16–31 is $188 \pm 44 \text{ W m}^{-2}$. The average ice cover is 17%. We define a heat flux at 100% ice cover, H_0 , by $H = H_0 P_i$, and find $H_0 = 1105 \pm 259 \text{ W m}^{-2}$.

Visually, the ice appeared to be rapidly melting in this region. We estimate the ice melt rate as $H_0/\rho_i L$, using a latent heat, L , and ice density, ρ_i , appropriate for -5°C , 7 psu ice. This yields ice melt rates of 37 ± 4 centimeters per day, comparable to the fastest summertime ice melt rates ever observed [*Morrison et al.*, 1987; *Josberger*, 1983].

Fig. 12

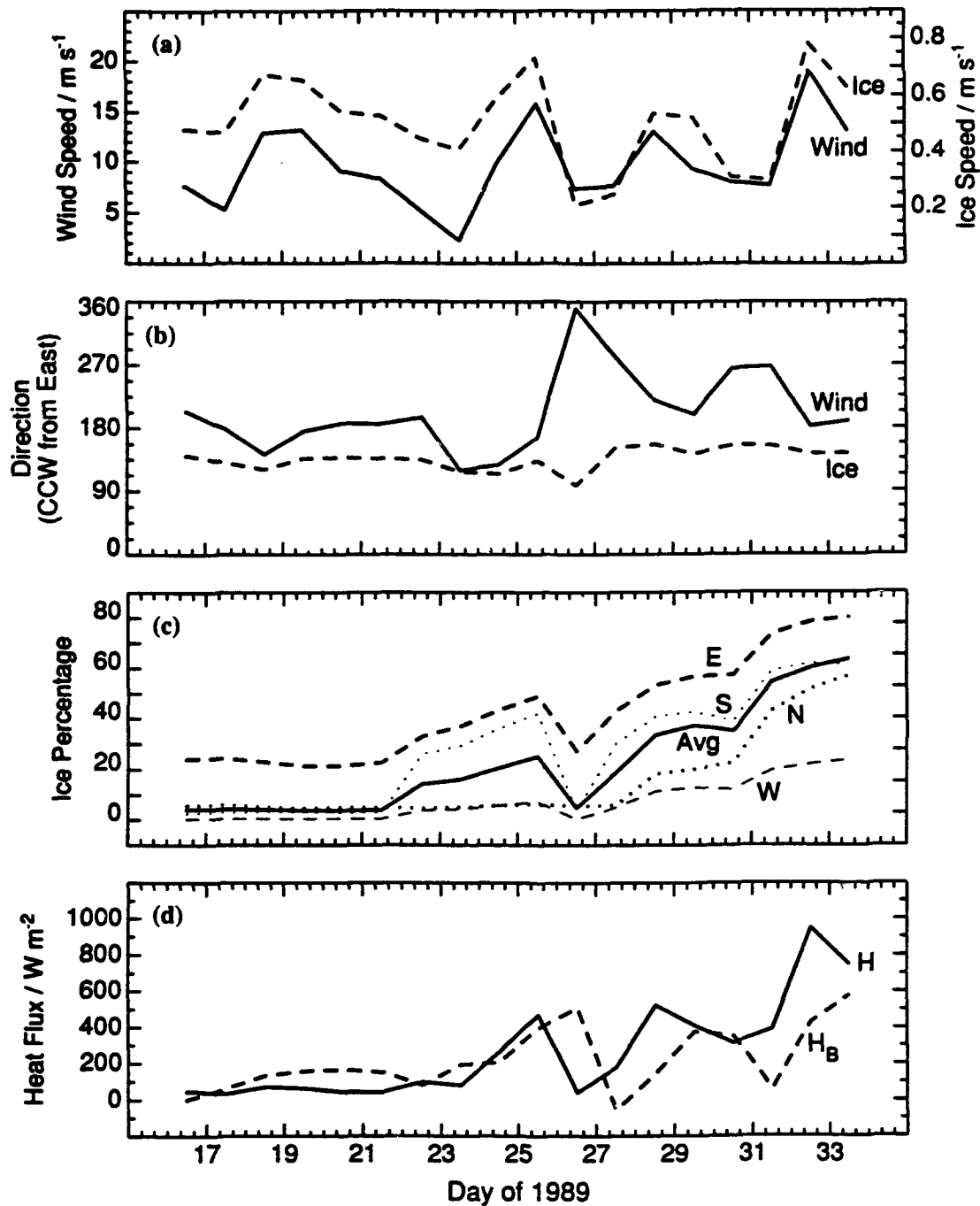


Fig. 12. Heat flux from the ocean to the ice. (a) Measured wind speed (solid curve) and resulting ice speed (dashed). (b) Wind and ice directions. (c) Average ice concentration in box (solid) and along the cardinal edges of the box (dashes and dots as labeled). (d) Heat flux to ice from ice melt model (solid) and from ice divergence model with an assumed ice thickness of 0.33 m (dashed). The heat flux to the ice increases as the ice concentration increases.

4.3. Sea Ice Advection

We check our estimate of ice melt rate by computing the mass balance of the ice in the same region. Figure 7 suggests that the oceanic currents vary little over our region, and we expect the wind also to be nearly uniform. We can therefore estimate the ice motion by a single, uniform velocity, v_i . We have little information on the ice thickness, h_i , so we also assume it to be uniform. A mass balance then yields an estimate of the local melt rate, H_B ,

$$H_B = -h_i \rho_i L_i \left[\frac{\partial P_i}{\partial t} + v_i \cdot \nabla P_i \right] \quad (8)$$

Daily maps of ice concentration from SSM/I, averaged both over the region (Figure 12c, solid) and at each of its edges (Figure 12c), allow both derivatives in (8) to be computed.

The ice motion was estimated from a free-drift model [McPhee, 1986], which assumes steady state and no ice interactions. If the ice is both sufficiently thin and moving sufficiently fast (for example, 1 m thick and 0.2 ms^{-1} , both of which apply to our case), then the momentum and the Coriolis force of the ice are negligible. The stress on the ice surface equals that on the bottom, and the ice moves at an angle $\beta = 23^\circ$ to the right of the wind (northern hemisphere) with relative speed

$$u_i = u_a \left[\frac{\rho_a c_{ai}}{\rho_w c_{iw}} \right]^{-1/2} \quad (9)$$

The air-ice and ice-water drag coefficients [McPhee, 1986] are $c_{ai} = 2.7 \times 10^{-3}$ and $c_{iw} = 5.5 \times 10^{-3}$, respectively, so that $u_i = 2.5 \times 10^{-2} u_a$. The ice motion (Figures 12a and 12b) is $v_i = u_i + \bar{v}$, where \bar{v} is the average surface velocity of the WSC (section 3.4).

By choosing an ice thickness of $h_i = 0.33$ m, H_B can be made to agree closely with H (Figure 12d). This thickness is consistent with our visual observations of mostly first-year ice and *Vinje's* [1985] compilation of the most common wintertime ice thickness (0.3–1.2 m) at Bjornoya. There is no contradiction between the ice heat budget (8) and the bulk ice heat fluxes (7).

These calculations indicate that the ice found over the WSC is advected from the Barents Sea, around the southern tip of Spitzbergen, and then northwestward over the WSC. We estimate $4.9 \times 10^3 \text{ m}^3 \text{ s}^{-1}$ of ice is advected into our study region across the southern and eastern boundaries, while $3.3 \times 10^3 \text{ m}^3 \text{ s}^{-1}$ melts while attempting to exit across the western boundary. The remainder exits across the northern boundary. *Vinje* [1985] estimated the 1970–1980 average January and February ice drift around the southern tip of Spitzbergen. Using his numbers and an ice thickness of 0.33 m yields an ice flux of $3.5 \times 10^3 \text{ m}^3 \text{ s}^{-1}$, comparable to our estimates.

4.4. *Heat Flux to the Atmosphere*

The heat flux to the atmosphere can be written as a sum of turbulent and radiative fluxes following *Pease* [1987]

$$Q = Q_s + Q_e - Q_{ld} + Q_{lu} \quad (10)$$

where the turbulent flux includes sensible, Q_s , and latent, Q_e , fluxes, and the radiative flux has upward and downward longwave components, Q_{lu} and Q_{ld} , respectively. The incoming shortwave radiation is negligible at this latitude in the winter. The

parameterization for the area average sensible heat flux is

$$Q_s = \rho_a c_a c_h u_a \overline{(T_a - T_w)(1 - P_i)} \quad (11)$$

in which $\rho_a = 1.3 \text{ kg m}^{-3}$ is the air density, $c_a = 1004 \text{ J kg}^{-1} \text{ }^\circ\text{C}^{-1}$ is the specific heat of air, and $c_h = 2 \times 10^{-3}$ is the sensible heat transfer coefficient. In the case of partial ice cover, Q_s and Q_e are nonzero only for the open water fraction, $1 - P_i$. We compute T_w from P_i (see appendix); it differs little from its average value of 0.97°C . For air temperatures between -5 and -10°C , the Bowen ratio (Q_s/Q_e) is between 1.7 and 2.3, so the sensible heat dominates. Since the uncertainty in the coefficients c_h and c_e results in uncertainties in Q which are larger than those due to the range of the Bowen ratio, we have fixed the Bowen ratio at 2, following Pease [1987]. The outgoing longwave radiation is $Q_{lw} = \sigma e_w T_w^4$, where $\sigma = 5.67 \times 10^{-8} \text{ W m}^{-2} \text{ }^\circ\text{C}^{-4}$ is the Stefan-Boltzmann constant and $e_w = 0.98$ is the emissivity of water. We approximate the backscattered longwave radiation as $Q_{ld} = \sigma e_a T_a^4$, where $e_a = 0.95$ is an effective emissivity for the air.

The results of these calculations are shown in Figure 13. Averaged over the period of oceanographic measurements (days 16–31), the area average heat fluxes are $Q_s = 171 \text{ W m}^{-2}$, $Q_e = 86 \text{ W m}^{-2}$, $Q_{ld} = -222 \text{ W m}^{-2}$, and $Q_{lw} = 307 \text{ W m}^{-2}$. The turbulent terms Q_s and Q_e dominate. The average total flux to the atmosphere is $Q = 341 \pm 36 \text{ W m}^{-2}$. The total surface heat flux $Q + H$ averages $529 \pm 56 \text{ W m}^{-2}$. Note that heat fluxes during the final storm (Figure 13), which terminated the oceanographic measurements, reach almost 1000 W m^{-2} for both Q and H , for a total heat flux of almost

Fig. 13

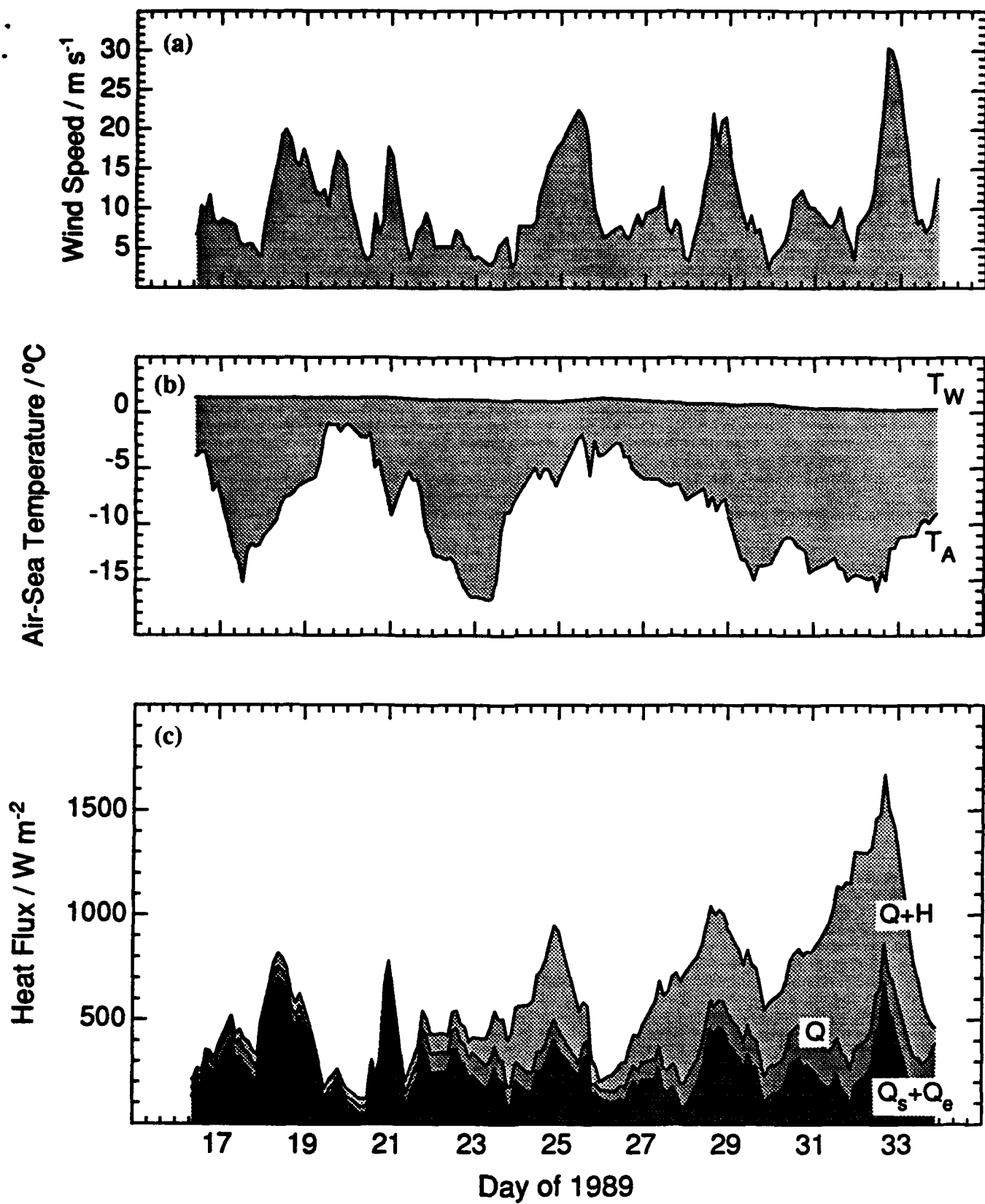


Fig. 13. Heat flux to the ice and atmosphere. (a) Wind speed. (b) Air temperature and water temperature. (c) Sensible and latent heat fluxes, $Q_s + Q_e$ (bottom line); total atmospheric heat flux Q (middle line); atmospheric and ice heat fluxes, $Q + H$ (top).

2000 W m^{-2} . The above averages do not include this storm. We note that these heat loss rates are comparable to *Häkkinen and Cavalieri's* [1989] January and February 1979 estimates of $400\text{--}600 \text{ W m}^{-2}$ for Q west of Svalbard and to *Untersteiner's* [1988] estimates of 300 W m^{-2} for H in northern Fram Strait.

4.5. *Heat Flux Summary*

The above calculations estimate a heat loss from our experimental area to the atmosphere of $Q = 341 \pm 36 \text{ W m}^{-2}$ and a heat loss to melting ice of $H = 188 \pm 44 \text{ W m}^{-2}$. These rms errors reflect only our statistical uncertainties. Much larger uncertainties exist in flux models we have used. These numbers reflect an average ice concentration of 17%. Totally ice-free regions have an average local heat flux $Q_0 = 411 \text{ W m}^{-2}$, while totally ice covered regions have an average local flux $H_0 = 1105 \text{ W m}^{-2}$.

5. WATER MASS TRANSFORMATIONS

Our calculations above indicate that both the atmosphere and the ice play an important role in cooling the WSC. Cooling by contact with the ice, however, produces fresh water, while cooling to the atmosphere does not. Quite different water mass transformations result.

5.1. Water Masses

Figure 14 plots individual, 20-m-sampled CTD data points for each of the sections in Figure 4. These correspond to the circles in Figures 4a–4e, not the smoothed contours. The type of symbol denotes the geographical location of the data as shown in Figures 4 and 6 (shelf '+'; slope warm core 'O'; slope cold '*'; Greenland Sea 'x'). Boxes define the water mass categories proposed by *Aagaard et al.* [1985].

Fig. 14

The warm core of the WSC ('O') consists entirely of Atlantic water (AW), reflecting its origins and its high (>34.9 psu) salinity. Water of the same salinity, but cooler, is called Lower Arctic Intermediate Water (LAIW) and exists mostly offshore of the WSC in the Greenland Sea. AW, when cooled, becomes LAIW, and when cooled further becomes Greenland Sea Deep Water (GSDW). We observed no GSDW.

Lines of data radiate outward toward cooler temperatures and fresher salinities from the warm core (Figures 14c–14e). Fresher and lighter than LAIW, this is mostly Arctic Surface Water (ASW). It is found mostly above the warm core, especially at $y = -25$ km. Inspired by *Moore and Wallace* [1988], we propose that these ASW water classes result from cooling of the warm core by a combination of ice and atmospheric cooling.

The salinity of a mass of water cooled by ice will decrease at a rate

$$\frac{dS}{dt} = \frac{H(S_i - S_w)}{L_i \rho_i \Delta Z} \quad (12)$$

where ΔZ is the depth to which the cooling extends and $S_i - S_w \approx 28$ psu is the difference in salinity between the ice and water. We depart from *Moore and Wallace* [1988], noting

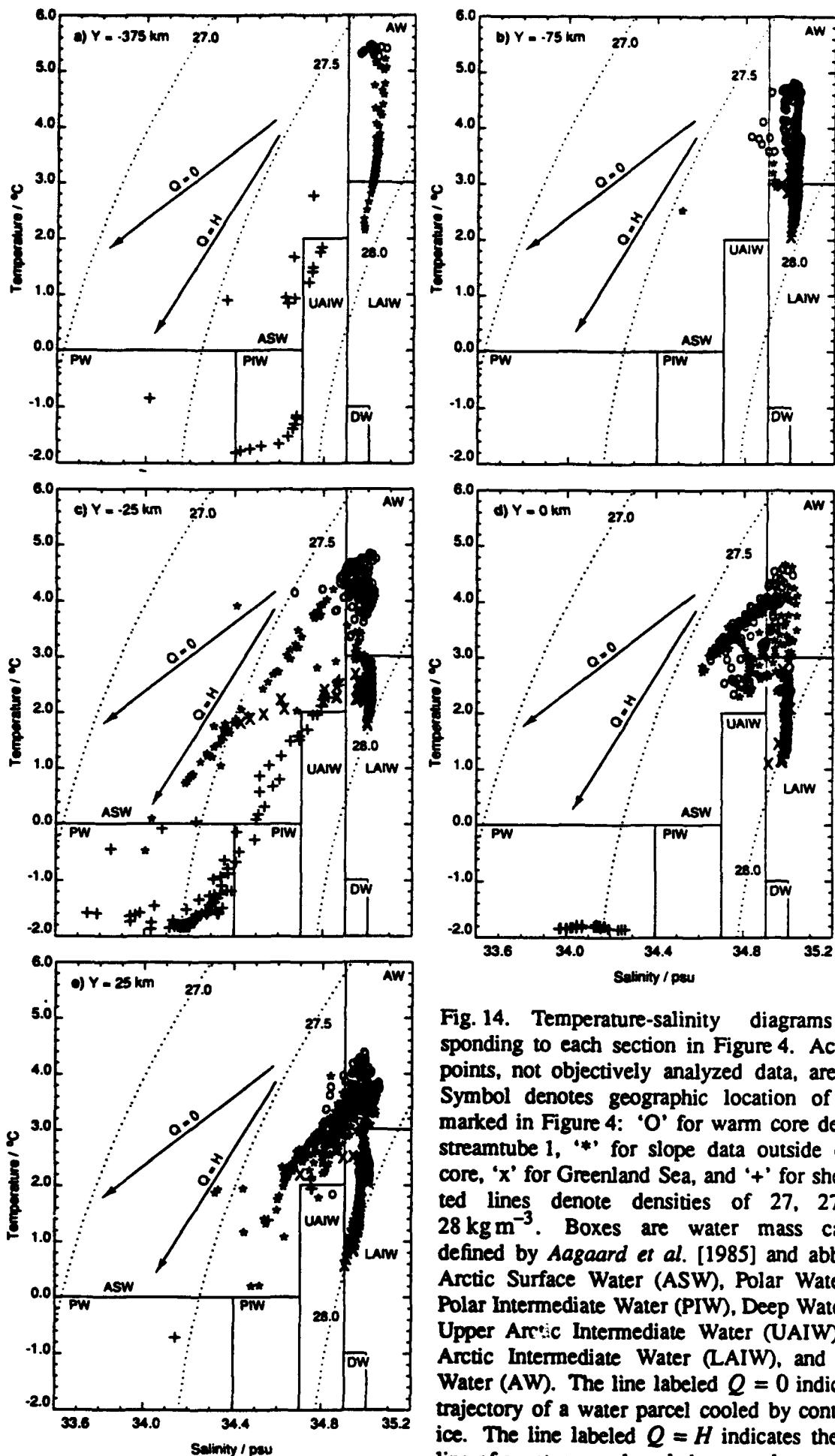


Fig. 14. Temperature-salinity diagrams corresponding to each section in Figure 4. Actual data points, not objectively analyzed data, are plotted. Symbol denotes geographic location of data as marked in Figure 4: 'O' for warm core defined by streamtube 1, '*' for slope data outside of warm core, 'x' for Greenland Sea, and '+' for shelf. Dotted lines denote densities of 27, 27.5, and 28 kg m⁻³. Boxes are water mass categories defined by *Aagaard et al.* [1985] and abbreviated Arctic Surface Water (ASW), Polar Water (PW), Polar Intermediate Water (PIW), Deep Water (DW), Upper Arctic Intermediate Water (UAIW), Lower Arctic Intermediate Water (LAIW), and Atlantic Water (AW). The line labeled $Q = 0$ indicates the trajectory of a water parcel cooled by contact with ice. The line labeled $Q = H$ indicates the mixing line of a water parcel cooled an equal amount by ice and the atmosphere.

that since the ice cover is never 100% in our study region, a water mass in contact with the ice will also be cooled by the atmosphere through nearby leads. Its temperature will thus decrease at

$$\frac{dT}{dt} = - \frac{Q+H}{\rho_w c_w \Delta Z} \quad (13)$$

where we have ignored the small amount of heat necessary to warm the ice from its ambient temperature to the freezing point, and the even smaller contribution of latent heat to salinity flux. The water mass will thus travel along a curve with a T/S slope of

$$\frac{dT}{dS} = \left[\frac{Q+H}{H} \right] \frac{\rho_i L_i}{\rho_w c_w (S_w - S_i)} \approx 2.85 \left(\frac{Q}{H} + 1 \right) \quad \left[\frac{^{\circ}\text{C}}{\text{psu}} \right] \quad (14)$$

The observed T/S slope thus corresponds to the Q/H ratio at the mass formation site, with a slope of 2.8 implying $Q/H = 0$. The value of Q/H , in turn, depends strongly on the ice concentration, with $Q = Q_0(1 - P_i)$ and $H = H_0 P_i$. Thus

$$P_i = \left[\frac{Q}{H} \frac{H_0}{Q_0} + 1 \right]^{-1} \quad (15)$$

For our data the time averaged heat fluxes imply $H_0/Q_0 \approx 2.7$.

The ASW classes in Figures 14a and 14e have T/S slopes of 4 to 6, corresponding to Q/H of 0.4 to 1.1 by (14) and ice concentrations at the water mass formation area of 25%–50% by (15). Although our average ice concentrations are much lower, averaging 17%, the average concentration of ice when the ice cover is greater than 10% is 43%, comparable to those found from the T/S properties. We therefore conclude that the cool-

ing of AW in regions of partial ice cover can produce ASW with the observed T/S slopes.

5.2. Salinity Structure

In Figure 15, salinity and density contours for each of the sections map the locations of the water masses. Water with $S > 34.85$ psu (light shading) is AW or LAIW and cannot have been in contact with ice. Water with $S < 34.85$ psu (heavier shadings) is ASW and must include some ice melt component.

Fig. 15

In general, LAIW is found on the offshore edge of the warm core and in the Greenland Sea, while ASW is found inshore and above the warm core, consistent with westward advection of ice over the WSC. If we arrange the sections chronologically, rather than by latitude, so that their order is -75 km (day 21), 25 km (days 20-23), 0 km (days 25-36), and -25 km (days 27-29), a nearly monotonic increase in ASW above the warm core appears. This corresponds nicely with the steady increase in ice (Figures 10-12) during the measurements. Thus the early sections (-75 km and 25 km) show little freshening by ice, while the later ones (0 km and -25 km) show prominent layers of fresh ASW caused by contact with ice. Although the temperature of the WSC decreases nearly monotonically northward (Figure 9b), the salinity depends on ice concentration, which, in these data, increases with time, not space.

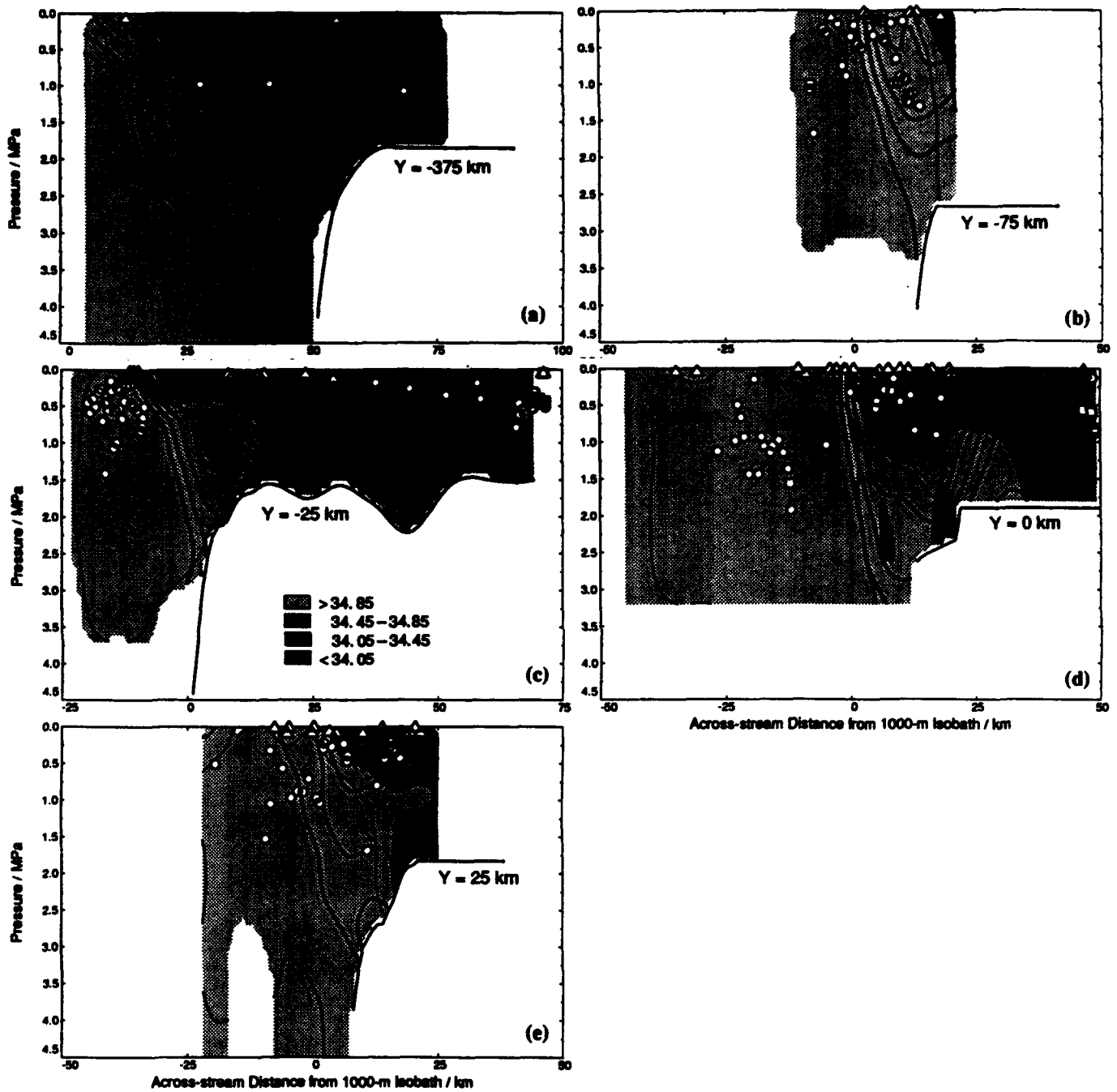


Fig. 15. Salinity structure for each section in Figure 4. Salinity contours with interval 0.1 psu are shaded. Water saltier than 34.85 psu has the lightest shading; this corresponds to the salinity of the incoming Atlantic Water. Density is contoured as in Figure 4. Mixed layer depths are indicated by the white symbols.

6. MIXED LAYER STRUCTURE

The white symbols in Figure 15 show the depth of the mixed layer for each section, defined as the first depth where the temperature gradient over 6 m exceeds 0.8° per 100 m. Figure 16 is an example of individual profiles from a CTD tow-yo with the estimated mixed layer depths marked. Figure 17 shows the estimated mixed layer depths for all profiles, including some not included in Figure 15.

Fig. 16

Fig. 17

In general, the mixed layer depths are shallowest over the warm core, deeper on the shelf, and deeper still in the Greenland Sea. At all locations, the mixed layer depths vary dramatically over short distances (Figure 16) and profiles with no mixed layer (triangles in Figures 15 and 17) are common, especially over the warm core. Except on the shelf, the mixed layers are warmer than the air and the freezing point (Figure 4). These are properties of very young mixed layers, actively exchanging heat and mass with the stratified interior. We quantify this below.

In ice-free regions, the average Q_0 , 411 W m^{-2} , acting on a 20-m-deep mixed layer would cool it 1°C in 2.5 days. Since the difference between the mixed layer temperature and that of the underlying ocean is usually much less than a degree (Figures 4 and 16), the water in the mixed layer has either been in contact with the atmosphere for less than 2 days or is heated strongly from below. This result also holds for the 2-day average Q_0 , which is never less than 293 W m^{-2} .

In partially ice covered regions, ice melt produces a strongly stratified surface layer of ASW and shallow mixed layers. These mixed layers, however, are warmer than the

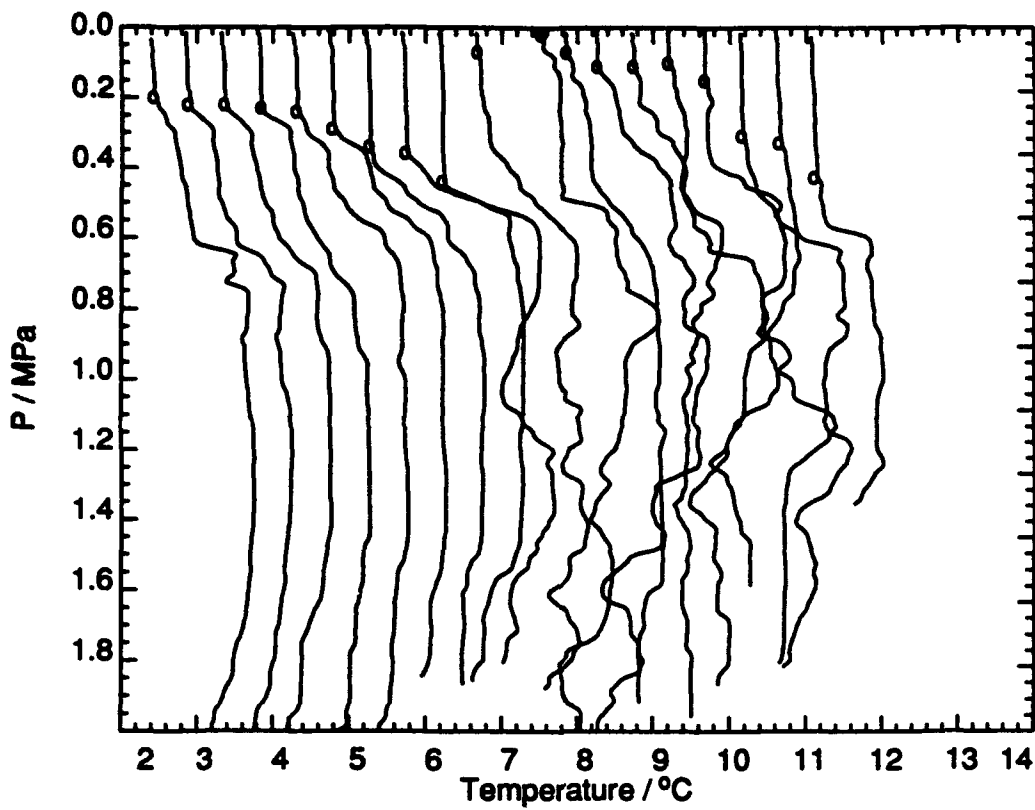


Fig. 16. Successive temperature profiles from tow-yo CTD profiling through the edge of the warm core near $y = 0$ km. The entire sequence is only about 6 km long. Note the extreme variability in this short distance.

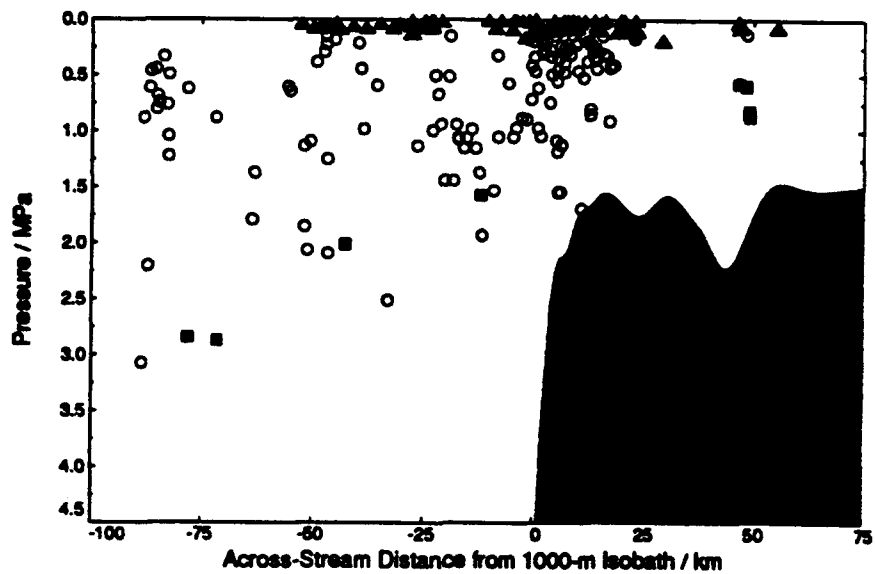


Fig. 17. Mixed layer depths from all CTD profiles plotted against across-stream distance. Triangles indicate no mixed layer; squares indicate a mixed layer deeper than the profile. Notice very shallow and variable mixed layers over the warm core.

freezing point; the coldest mixed layer found off the shelf is -0.7°C , a degree above the freezing point. With an average ice cover in ASW formation regions of 30%, and the values of Q_0 and H_0 above, a typical surface heat flux in these regions is 600 W m^{-2} . This would cool a 10-m mixed layer 1°C in about 18 hours. Thus the under-ice mixed layers must either be less than a day old or be strongly heated from below.

The strong surface forcing in this region implies a rapid mixed layer growth. We use a very simple version of the *Kraus and Turner* [1967] model in which a wind-forced mixed layer grows into an initially uniform stratification N^2 . This model is appropriate for the very shallow mixed layers found here. For constant wind stress u^* applied for time t , the mixed layer has a depth [Turner, 1973, 9.2.3]

$$H_{ml} = u^* \left[\frac{15m_0}{N^2} t \right]^{\frac{1}{3}}. \quad (16)$$

We use a mixing efficiency $m_0 = 0.6$ following *Davis et al.* [1981]. Other published values range from 0.23 to 50 [Huang, 1986]; those based on oceanographic data range from 0.23 [Wu, 1973] to 1.2 [Niller, 1977]. This range leads to only a 50% uncertainty in H in (16) due to the $1/3$ power. We use $N^2 = 10^{-5} \text{ s}^{-2}$, appropriate to the WSC warm core. In the Greenland Sea, a smaller value would be appropriate; in the most highly stratified ASW layer (Figure 4c), a value 10 times larger would apply. Wind speed was usually within 50% of 9 m s^{-1} while CTD profiles were being made. We estimate the drag coefficient as between 1.2×10^{-3} for open water and 2.5×10^{-3} for rough ice. From

these we estimate u^* within a factor of 2 of 0.013 m s^{-1} .

Using these values (16) predicts a mixed layer growth of 55 m in one day, 19 m in 1 hour, and 3 m in 100 seconds, all with a factor of 3 possible error. Since mixed layers shallower than 20 m are common, we conclude that these must either be younger than a day or be subject to an upwelling of at least 20 m per day. In either case, there must be a strong exchange between the surface and the interior. We note that (16) does not include the effects of buoyancy forcing in deepening the mixed layer. Away from ice, we estimate the characteristic buoyancy velocity scale w^* as $w^{*3} = gQ\alpha H_{ml}/\rho C_w$, where α is the expansion coefficient of seawater [Stull, 1988]. For $H_{ml} = 20 \text{ m}$ and $Q = 500 \text{ W m}^{-2}$, we find $w^* = 0.01 \text{ m s}^{-1}$, comparable to u^* . Equation (16) therefore underestimates H_{ml} by somewhat less than a factor of 2, well within the other uncertainties.

These considerations all imply exchange of heat and mass between the upper 102–220 m and the deeper, stratified interior with a time scale faster than a day over the WSC. Near the surface, this must either occur by rapid upwelling, balanced by rapid downward growth of the mixed layer, or by subduction of the mixed layers into the stratification, as suggested by Figure 16. In contrast, the deep mixed layers over the Greenland Sea imply downward growth of the mixed layer unimpeded by these other processes.

7. MIXING MECHANISMS

7.1. *The Question*

At our southernmost section (Figure 4a) the warm core extends into a mixed layer. It can therefore be cooled directly by the atmosphere in the traditional way. Farther north, however, the mixed layers are shallow, and the warm core is separated from the surface by about 0.1 kg m^{-3} of stratification. Nevertheless, it continues to cool (Figure 9) at a very rapid rate (Table 2). How can this happen?

7.2. *Isopycnal Diffusion by Mesoscale Eddies*

Energetic mesoscale eddies fill the entire northern Greenland Sea, including the WSC [Gascard *et al.*, 1988; Johannessen *et al.*, 1987]. The largest of these have radii of 15 km and speeds of up to 0.5 m s^{-1} . These are also present, although poorly resolved, in our data. Comparison of the raw temperature (circles) and the smoothed contours in Figure 3 or 4 reveals abundant small scale variability. Figure 16 shows an example of the resulting complex hydrographic structure. Figure 6 shows evidence of a larger eddy near $y = 0 \text{ km}$, perhaps associated with the nearby canyon extending onto the shelf.

A mesoscale eddy field will diffuse properties along mean isopycnals [Haidvogel and Keffer, 1984]. Since the isopycnals passing through the WSC warm core outcrop 5–10 km west of the core (Figure 4), the mesoscale eddy field will transport heat from the warm core to the surface. Parcels of warm WSC water will be moved to the surface, while parcels of cooler surface water will be moved back to the warm core. The net

result will be a heat flux from the warm core, diagonally along isopycnals to the ocean surface.

We model the isopycnal heat flux, Q_I , using an isopycnal diffusivity, K_I ,

$$\frac{Q_I}{\rho c_w} = u' T' = K_I T_{lx} \quad (17)$$

$$K_I = u' l'$$

where the eddy heat flux K_I is written in terms of characteristic eddy velocity u' and length l' scales [Böning, 1988]. Consistent with this model, the isopycnals connecting the warm core to the surface cool toward the surface (Figures 4b–4e) with a gradient of $T_{lx} = 0.8\text{--}2.0 \times 10^{-4} \text{ }^\circ\text{C m}^{-1}$, as expected if heat is diffusing from the warm core to the surface. Below the warm core, along the same isopycnals, there is little temperature gradient. We estimate from streamtube 2 that the warm core cools at about $5 \times 10^6 \text{ W m}^{-1}$. The streamtube height is about 165 m, T_{lx} is about $10^{-4} \text{ }^\circ\text{C m}^{-1}$, so $Q_I = 3 \times 10^4 \text{ W m}^{-2}$. This heat is lost out the side of the warm core. Using (17), $K_I = 74 \text{ m}^2 \text{ s}^{-1}$. From Figure 6, we expect u' to be somewhat less than \bar{v} , say within a factor of 2 of 0.05 m s^{-1} ; this implies a diffusion length scale l' within a factor of 2 of 1.4 km. The associated temperature fluctuations, $T' = T_{lx} l'$, are about $0.1 \text{ }^\circ\text{C}$.

These calculations imply that all of the heat flux necessary to cool the warm core could be carried by isopycnal diffusion by a mesoscale eddy field with l' of about a kilometer and T' of about 0.1° . Both numbers seem quite reasonable. Temperature fluctuations of this magnitude are common in our data. In the North Atlantic, Böning

[1988] finds l' of 45–80 km, comparable to the local Rossby radius. Our value is much smaller, but so is the Rossby radius. Although we do not have sufficient information for a detailed study of mesoscale eddies in this region, it appears that they can easily transport the heat necessary to cool the warm core of the WSC.

The highly variable mixed layers found in the WSC can also be plausibly due to mesoscale eddies. The residence time of surface water should be comparable to the eddy time scale, l'/u' , which is somewhat less than a day, using the above values. The isopycnals rise about 120 m from the warm core to the surface in about 8 km horizontally (Figures 4b–4e). This slope implies typical eddy vertical velocities w' of roughly 64 m per day. Both of these estimates are similar to those estimated independently from the mixed layer characteristics.

7.3. *Diapycnal Diffusion by Turbulence*

Diffusion across isopycnals by small scale turbulent mixing [Gregg, 1987] could also be important in cooling the warm core. The heat flux required to cool the warm core (streamtube 2) $Q_D \approx 800 \text{ W m}^{-2}$ is equivalent to a diapycnal diffusivity

$$K_D = \frac{Q_D}{\rho_w c_w T_z} \quad (18)$$

where T_z is the typical temperature gradient between the warm core and the surface. For the two southernmost sections (Figures 4a and 4b), the mixed layer reaches almost to the warm core, and T_z is very small. For the three northern sections (Figures 4c–4e), the

temperature gradient varies from $0.006^{\circ}\text{C m}^{-1}$ to $0.017^{\circ}\text{C m}^{-1}$, corresponding to K_D values of $3 \times 10^{-2} \text{ m}^2 \text{ s}^{-1}$ to $1 \times 10^{-2} \text{ m}^2 \text{ s}^{-1}$. These are much larger than typical diffusivities in the oceanic thermocline, $10^{-5} - 10^{-4} \text{ m}^2 \text{ s}^{-1}$ [Gregg, 1989]. Padman and Dillon [1991] infer a maximum sustained $K_D = 2.5 \times 10^{-4} \text{ m}^2 \text{ s}^{-1}$ in the WSC over the Yermak Plateau, about 400 km north of our area at comparable depth and stratification. These measurements, however, were made in a region of intense diurnal tides [Padman *et al.*, 1992] and are greatly elevated above the usual levels for this area [D'Asaro and Morison, 1992]. From these considerations alone, the diapycnal diffusivity seems unlikely to be large enough to cool the warm core.

Oceanic diffusivities are commonly predicted from estimates of the turbulent kinetic energy dissipation ϵ by

$$K_D = 0.2 \frac{\epsilon}{N^2} \quad (19)$$

[Gregg, 1987]. Substituting this into (18), we find the dissipation necessary to support the estimated cooling of the WSC core

$$\epsilon_Q = \frac{Qg \Delta\rho}{\rho_w c_w 0.2\rho_w \Delta T} \quad (20)$$

where ΔT and $\Delta\rho$ are the temperature and density changes used to compute N^2 and T_z . For the northern three sections, (19) yields ϵ_Q within a factor of 2 of $8 \times 10^{-7} \text{ W kg}^{-1}$. Integrated from the warm core to the surface, the total energy dissipated is within a factor of 2 of 0.06 W m^{-2} .

Could the wind supply the necessary energy? The power put into the ocean by the wind is $\rho_w u_*^3$, which for our wind data is 0.004 W m^{-2} for an open water drag coefficient of 1.2×10^{-3} and 0.012 W m^{-2} for a marginal ice zone drag coefficient of 2.5×10^{-3} . Much of the rest is certainly dissipated very near the surface [Oakey and Elliot, 1982], leaving perhaps 50% for diapycnal mixing below the mixed layer. The wind can plausibly supply only about $6 \times 10^{-3} \text{ W m}^{-2}$ for diapycnal mixing, an order of magnitude less than is required.

Gregg [1989] finds that ϵ correlates well with shear measured at a 10-m scale. Combining this with (19) he finds

$$K_D = 0.05 \left[S_{10}^2 / N^2 \right]^2 \quad (21)$$

where S_{10}^2 is the shear spectrum integrated to 10-m wavelength, or computationally, 2.11 times the shear variance computed from a least squares fit to 10 m of velocity data. We apply (21) to our nine XCP profiles being careful to remove biases and bad data due to noise, as described by D'Asaro and Morison [1992]. We obtain N^2 from the CTD profile closest to each XCP profile. The resulting estimates of K_D are highly variable both within a given profile and between profiles, so we are reluctant to draw any but the broadest conclusions. We reject three profiles as having a poor match between the CTD and XCP temperatures, and we reject the upper 100 m of all but three due to either very low, and thus poorly determined, N , or a suspicion of significant surface wave contamination. The remaining seven estimates range from $1.4 \times 10^{-4} \text{ m}^2 \text{ s}^{-1}$ to $12 \times 10^{-4} \text{ m}^2 \text{ s}^{-1}$, with a mean

of $6 \times 10^{-4} \text{ m}^2 \text{ s}^{-1}$. The three profiles with sufficient believable data above 150 m average $20 \times 10^{-4} \text{ m}^2 \text{ s}^{-1}$. *Wijesekera et al.* [1992] find that (21) underestimates K_D by about a factor of 4 in the strongly tidally forced region of the Yermak Plateau, so a value of $K_D = 10^{-3} \text{ m}^2 \text{ s}^{-1}$ is plausible. The WSC has very high shear levels by normal oceanic standards, and probably very high levels of diapycnal mixing, but these are probably not high enough to cool the warm core.

The high resolution CTD section in Figure 16 shows the mixed layer penetrating intermittently to just above the warmest water of the profile. This suggests that mixed layer entrainment can, at times, act directly on the warm core, thus cooling it. This may be more efficient than the above energetic argument suggests, thus enhancing the role of diapycnal mixing. A more detailed study of these processes, including data from simultaneous microstructure measurements, will be presented in a later paper.

8. SUMMARY

We have investigated the heat budget and water mass transformations in the West Spitzbergen Current based on data from a 3-week cruise in late January and early February of 1989. From these we can calculate several terms in the heat budget and describe how water mass transformations occur in this area. Our data are incomplete and aliased by both mesoscale eddies and temporal variations. As a result, most of our calculations are quite crude; the best have uncertainties close to 50%; others are only order-of-magnitude estimates. Nevertheless, air-sea interaction and water mass transformation

rates are so large in this area that we can obtain many meaningful results.

8.1. *Results*

Velocity structure. The WSC flowed northward parallel to the 1000-m isobath. Its speed varied little across our experimental domain, averaging $0.35 \pm 0.1 \text{ m s}^{-1}$ at the surface and decaying toward the bottom. The Ekman transport superimposed on this flow is approximately downstream and is less than 0.01 m s^{-1} averaged over 200 m depth.

Hydrographic structure. On horizontal scales smaller than 10–20 km, the WSC displayed a complex structure, with numerous interleaving intrusions and eddies. Averaging over these, a simpler structure emerged. A core of warm water centered just inshore of the 1000-m isobath was bounded on the offshore side by a density front separating it from the colder waters of the Greenland Sea and on the inshore side by the colder, fresher waters of the Spitzbergen shelf. Isopycnals connected the warm core to the surface on the Greenland Sea side. The warm core cooled at about 0.5°C per 100 km from Bjornoya at 74.5°N to the Yermak Plateau at 81°N . This same temperature gradient existed within our experimental region at about 77°N .

Heat fluxes from the ocean. The downstream cooling of the warm core implied a heat flux out of the core of about $2 \times 10^7 \text{ W m}^{-1}$, within a factor of 2. The actual value depended on how the warm core was defined. A vertical heat flux of 900 W m^{-2} from the approximately 22 km wide warm core to the surface could accomplish this cooling. The

total heat flux out of the WSC is significantly higher, since water outside of the warm core also cools.

Heat fluxes to the air and ice. The average heat flux to the atmosphere from open water regions was $341 \pm 36 \text{ W m}^{-2}$. An average of 17% of this region was covered by melting ice which absorbed $188 \pm 44 \text{ W m}^{-2}$. These averages are over the duration of our measurements and over a $50\text{-km} \times 100\text{-km}$ region which approximately defines the spatial extent of the measurements.

Ice dynamics. The ice advected over the WSC originated in the Barents Sea and was dominantly first-year ice. Advection of the ice by the measured wind was consistent with the estimated ice melt rate over the WSC if the ice thickness was 0.33 m, a reasonable value.

Mixed layer properties. The mixed layer depths were extremely variable and often very shallow over the warm core. This implied active exchange of surface water with the interior, with a typical exchange time of less than a day.

Water mass transformations. The Atlantic Water contained in the warm core was cooled both by atmospheric heat flux and by melting ice. Atmospheric heat flux alone converted Atlantic Water to cold, relatively salty Lower Arctic Intermediate water. Cooling to ice converted the Atlantic Water to cold but fresher Arctic Surface Water (ASW). The T/S slope of the ASW implied roughly equal contributions from air and ice, which, in turn, implied an ice concentration in the areas of ASW formation of roughly

25-50%.

Heat transport mechanisms. The warm core is often separated from the surface by stratification. In this case, diapycnal diffusion cannot carry the large heat fluxes necessary to cool the warm core. Diffusion by eddies along the isopycnals which connect the warm core to the surface is the likely mechanism.

8.2. *Synthesis*

Figure 18 summarizes a model of the heat budget and water mass transformations consistent with our data. The warm core of the WSC cools in three ways.

Fig. 18

Direct atmospheric cooling, Region I. In the southern part of our survey region, the warm core reaches the surface. Its upper part consists of a warm, deep mixed layer which is cooled directly by the atmosphere. The Atlantic Water is cooled at nearly constant salinity, transforming it into Lower Arctic Intermediate Water. The mixing is due to turbulence in the mixed layer, driven by waves and atmospheric heat and momentum fluxes.

The cooling rate is governed by the atmospheric heat flux which, for our data, averages about 400 W m^{-2} . This will convert 0.5 Sv of 5°C AW to 3°C LAIW along the 25-km \times 400-km path from Bjornoya to 78°N .

Direct ice cooling, Region II. Further north, ice is advected over the warm core from the Barents Sea, resulting in dramatic cooling and freshening of the surface. This

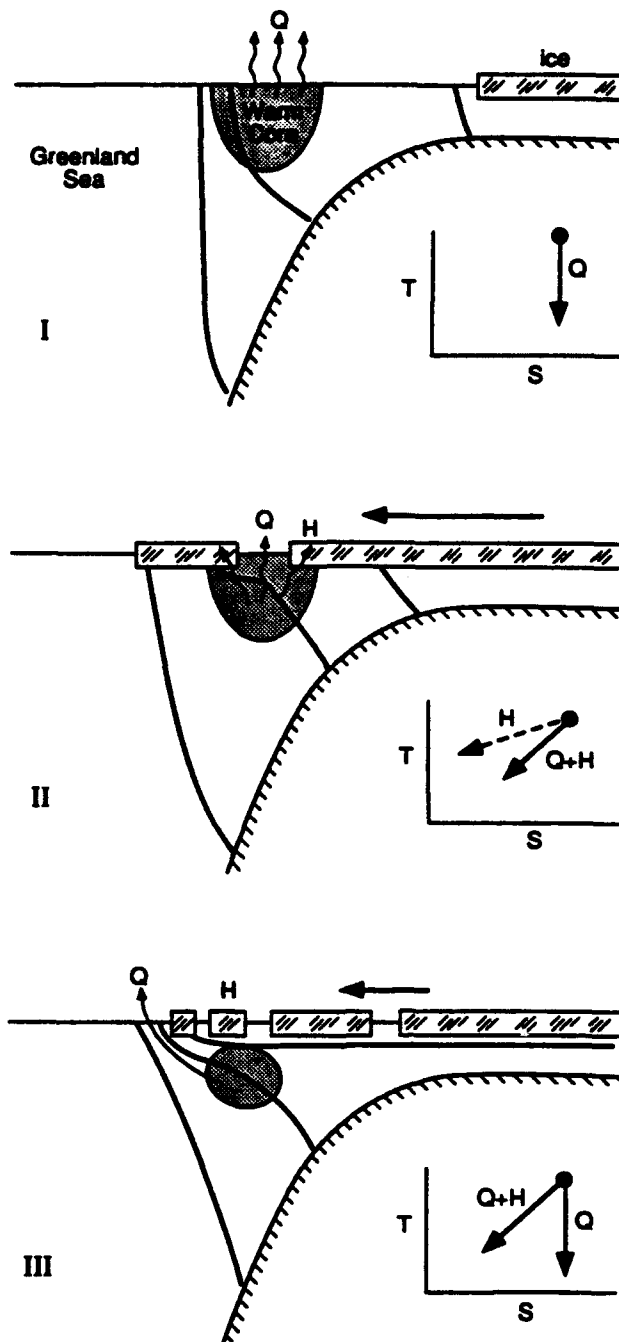


Fig. 18. Conceptual stages in the cooling of the warm core of the West Spitzbergen Current. I. Cold air directly cools the warm core producing cold, salty water. II. Ice advects over the warm core and melts, directly cooling and freshening it. Cold air continues to cool the warm core though leads. Cold, but fresher water is produced. III. Cold fresh water covers warm core. Cooling continues, however, via mixing along the isopycnals which connect the warm core to the surface. The ice edge intermittently advects over this outcropping, so that both cold salty water and cold fresh water are produced.

results in the conversion of Atlantic Water to Arctic Surface Water. The T/S characteristics of the ASW are controlled by the relative contribution of ice melting and atmospheric cooling. The mixing is due to boundary layer turbulence driven by ice motion, as well as wind and waves. The resulting strong surface stratification must partially insulate the warm core from further surface mixing.

The cooling rate is governed primarily by the rate at which ice is advected over the WSC by the wind. We estimate about $0.04 \text{ m}^3 \text{ s}^{-1}$ of ice per downstream meter entered our experimental region, sufficient to cool 0.6 Sv of 4°C Atlantic Water to 0° ASW along the approximately 400 km of Spitzbergen Shelf. This estimate includes an equal heat loss to the atmosphere in the partially ice-covered formation zone.

Isopycnal mixing, Region III. The maximum temperatures of the warm core continue decreasing even after it is isolated from the surface by ASW. We attribute this primarily to mixing of water from the warm core to the surface offshore of the ASW by isopycnal, eddy driven mixing. Diapycnal mixing may also play a role. In our observations, the isopycnal mixing appears to form LAIW on the offshore, and still ice-free, edge of the warm core.

The cooling rate is probably controlled by the dynamics of the eddy field and the structure of the isopycnals. Surprisingly, the warm core cools at approximately the same rate after it is covered by ASW as before, suggesting that the eddy fluxes and the surface cooling rates are intimately connected. Our estimates indicate that the local heat loss of

the WSC is larger than the local heat gain by air and ice. This indicates that heat lost by the WSC is spread horizontally over several times its width before being lost to the atmosphere and ice. A closer look at the dynamics of this system is needed to understand these features.

9. DISCUSSION

9.1. *Sensitivity of Water Mass Conversions*

The processes described here control the conversion of warm Atlantic Water into either cold, fresh Arctic Surface Water or cold, salty Lower Arctic Intermediate Water. Only the latter can be further cooled to form the deep and intermediate waters that spill out of the Iceland and Greenland Seas [*Swift and Aagaard, 1981*]. This study indicates that the balance between the production of ASW and LAIW is highly sensitive to details of the regional oceanography.

The most important factor locally appears to be the rate at which first-year ice is advected from the Barents Sea over the WSC. If there were no ice, all of the AW would be converted to LAIW. The ice advection, in turn, depends on the local wind fields, the seasonal cooling rate over the Barents Sea, and the geometry of the Spitzbergen Islands. It is particularly striking that the main Arctic ice pack to the north appears to play no role. This would seem to imply that if additional islands blocked the flow of ice from the Barents Sea more LAIW water would be produced, with perhaps a corresponding

increase in deep convection.

A second factor is the lack of an upwelling circulation. During our measurements, the average wind was from the east, so the average Ekman transport was along-shore northward. A more northerly wind would rotate the Ekman transport offshore, leading to an upwelling circulation which might bring the warm core more directly in contact with the surface. This would enhance the water mass conversion rate, leading to less transport of heat into the Arctic Ocean and more local heat loss. Whether this would lead to more ASW production, more LAIW production, or more of both and less heat export to the Arctic Ocean is unclear.

A third factor is the mesoscale eddy field. This acts to continue the cooling of the WSC after it is capped over by ASW by diffusing water isopycnally around the ASW cap. Otherwise, cooling of the warm core would presumably stop after its first encounter with ice. It seems likely that the details of the eddy field are sensitive to the local topography as well as the structure of the WSC. Additional dynamical insight would be helpful in understanding these processes.

An example of the sensitivity of water mass conversions in this area to interannual variability is given by *Aagaard et al.* [1987], who made similar, but less extensive, measurements just north of Svalbard. At the time, November 1977, this area was entirely ice free. As expected, their data showed conversion of AW to LAIW with little production of ASW. Similar variability is also found seasonally, as the ice cover increases

throughout the winter season. Early in the winter, with light ice cover, production of LAIW should predominate; later in the winter, ASW production should dominate. The steady increase in ice coverage during our measurements may reflect this seasonality.

9.2. *Conversion and Circulation*

Aagaard et al. [1987], *Manley et al.* [1992], and *Gascard et al.* [1988], among others, suggest that the WSC splits into several filaments just north of our study region. The inshore branch follows the shelf break around Spitzbergen, the central branch follows the edge of the Yermak Plateau into the Arctic Ocean, and the outer branch follows the fracture zones across Fram Strait to recirculate into the Greenland Sea. This recirculating water is most likely to be further cooled to form Deep Water [*Quadfasel and Meincke*, 1987]. There is no evidence of separate cores in our data, so this fragmentation must occur farther north, where the topography becomes more complex.

Figure 15 suggests that conversion of AW to ASW is concentrated on the inshore side of WSC, where the ice concentration is higher, while conversion to LAIW occurs on the offshore edge. We speculate that the ASW is more likely to follow the inner branches of the WSC into the Arctic Ocean, while the LAIW is more likely to recirculate. This tends to keep the fresh ASW away from the deep convection regions, where it can inhibit convection. If the ice originated on the western, rather than eastern side of the current, the opposite sorting might occur, and the fresher of the two water masses would be sent to the convection region. This again emphasizes the sensitivity of these water mass

conversion processes to seemingly small details.

Arctic Surface Water with T/S slopes and salinities similar to those found here was observed in the vicinity of the Yermak Plateau by *Perkin and Lewis* [1984] and *Muench et al.* [1992]. *Perkin and Lewis* [1984] observe multiple intrusions with different temperatures, much as seen here. They attribute these to double-diffusive mixing near the Yermak Plateau, while *Muench et al.* [1992] attribute it to mixing between AW and Upper Arctic Intermediate Water. We suggest, rather, that this water is formed in the WSC by the combined action of ice and atmospheric heat flux. The multiple cores are formed by cooling different temperatures of AW at different locations and times along the WSC. Cooled to the freezing point, ASW formed in this way is nearly identical to the halocline water of the eastern Arctic. We therefore see no need to form the eastern Arctic halocline by salinization on the shelves. It can be formed from Atlantic Water which has been cooled by the atmosphere, and cooled and freshened by ice.

APPENDIX: BULK FORMULA FOR THE AVERAGE HEAT FLUX TO ICE

McPhee [1987] provides a parameterization for the ice-water heat flux at a point

$$H = \rho_w c_w c_h u_* (T_w - T_f), \quad (\text{A1})$$

where $\rho_w c_w = 4.2 \times 10^6 \text{ J m}^{-3} \text{ }^\circ\text{C}^{-1}$, $c_h = 5.5 \times 10^{-3}$, u_* is the friction velocity at the ice-water interface, T_w is the mixed layer temperature, and T_f is the freezing temperature, a weak function of salinity. We use the value for 33 psu. We wish to estimate the areal average heat flux in a region with great variation in the ice concentration P_i . With

the overbar indicating an areal average.

$$\overline{H} = \rho_w c_w c_h \overline{u_* (T_w - T_f) P_i} \quad (\text{A2})$$

Evaluating (A2) requires estimating T_w over a wide region. In the along-track data from the *Polarbjorn*, P_{ip} and T_w are correlated, with $r = -0.54$. We found warmer water where the ice concentration was low and colder water where it was high, which makes sense if the ice concentration is primarily controlled by melting due to a large heat flux from the ocean. We thus compute T_w from P_{is} using the correlation of T_w and P_{ip} . The average of T_w is $1.50 \pm 0.05^\circ\text{C}$.

For thin ice, the Coriolis force is negligible and the air-ice stress, τ_{ai} , equals the ice-water stress, τ_{iw} [McPhee, 1986]. The friction velocity at the ice-water interface required in (A2) is then $u_* = (\rho_w^{-1} \rho_a c_{d(ai)} u_{ai}^2)^{1/2}$, where $c_{d(ai)}$ is the air-ice drag coefficient and u_{ai} is the wind speed. Drag coefficients over sea ice are observed to increase with both ice concentration and ice roughness (e.g., Anderson [1987] and Guest and Davidson [1987]). Typical values range from $2-3 \times 10^{-3}$. We have used a value of $c_{d(ai)} = 2.5 \times 10^{-3}$ in (A2), corresponding to an upwind concentration of rough floes of about 40%, from Guest and Davidson [1987]. The daily vector averaged wind, u_{ai} , is assumed to be spatially uniform. The average daily wind speed of 10.3 m s^{-1} results in an average friction velocity of 1.8 cm s^{-1} .

The melt rate of the ice can be obtained directly from the heat flux as

$$w_{ice} = H (\rho_i L_i)^{-1} \quad (A3)$$

where ρ_i is the density of the ice and $L_i = 2.67 \times 10^5 \text{ J kg}^{-1}$ is heat of fusion of 7-psu ice at a temperature of 5°C [Maykut, 1985]. This salinity is typical of first-year ice, and the temperature is the mean of the interfacial temperature of about -1.7°C and the average air temperature of about -9°C .

Acknowledgments. This work was part of the Coordinated Eastern Arctic Experiment (CEAREX). Special thanks to Andy Heiberg, who handled the CEAREX logistics, for allowing us an extra week for our measurements. The hard work of taking these data under unpleasant conditions was done by Pat McKeown, Susan Frankenstein, Tom Lehman, Suzanne O'Hara, and Jay Ardai. Bill Crawford selflessly offered us helpful advice on how to build our free-fall CTD; Mike Welch constructed it. Carol Pease and Wade Blake helped with the meteorological data. SSM/I data were provided by the National Snow and Ice Data Center, Boulder. Finally, the crew of the *Polarbjorn*, despite sickness, bad weather, and our ignorance of Norwegian, was a model of good seamanship and good advice. This work was supported by ONR contract N00014-87-K-0004 and Grant N00014-91-J-1405.

REFERENCES

- Aagaard, K., and E. C. Carmack, The role of sea ice and other fresh water in the Arctic circulation, *J. Geophys. Res.*, *94*, 14,485–14,497, 1989.
- Aagaard, K., and P. Greisman, Toward new mass and heat budgets for the Arctic Ocean, *J. Geophys. Res.*, *80*, 3821–3827, 1975.
- Aagaard, K., J.H. Swift, and E. C. Carmack, Thermohaline circulation in the Arctic mediterranean sea, *J. Geophys. Res.*, *90*, 4833–4846, 1985.
- Aagaard, K., A. Foldvik, and S.R Hillman, The West Spitzbergen Current: Disposition and water mass transformation, *J. Geophys. Res.*, *92*, 3778–3784, 1987.
- Anderson, R. J., Wind stress measurements over rough ice during the 1984 Marginal Ice Zone Experiment, *J. Geophys. Res.*, *92*, 6933–6941, 1987.
- Böning, C. W, Characteristics of particle dispersion in the North Atlantic: An alternative interpretation of SOFAR float results, *Deep Sea Res.*, *35*, 1379–1385, 1988.
- Bretherton F.P., R.E. Davis, and C.B. Fandry, A technique for objective analysis and design of oceanographic experiments applied to MODE-73, *Deep Sea Res.*, *23*, 559–582, 1976.
- Christou, N. T., Evaluation of mathematical models for gyrocompass behavior: Error modelling and applications, Dept. of Surveying Engineering, University of New Brunswick, Fredericton, 1983.
- D'Asaro, E. A., and J. H. Morison, Internal waves and mixing in the Arctic Ocean, *Deep Sea Res.*, *39*, Suppl. 2, S459–S484, 1992.

- D'Asaro, E. A., T.B. Sanford, R.G. Drever, M.D. Morehead, and G.L. Welsh, Air expendable current profiling during the OCEAN STORMS experiment, *APL-UW TR 8916*, Appl. Phys. Lab., Univ. of Wash., Seattle, 1990.
- Davis, R. E., R. DeSzoeko, D. Halpern, and P. Niiler, Variability in the upper ocean during MILE, Part II: Modeling the mixed layer response, *Deep Sea Res.*, 28, 12A, 1453–1475, 1981.
- Dietrich, G. (compiler), *Atlas of the Hydrography of the northern North Atlantic Ocean*, Conseil International Pour L'Exploration de la Mer, Service Hydrographique, 1969.
- Gascard, J.-C., C. Kergomard, P.-F. Jeannin, and M. Fily, Diagnostic study of the Fram Strait marginal ice zone during summer from 1983 and 1984 Marginal Ice Zone Experiment Lagrangian observations, *J. Geophys. Res.*, 93, 3613–3641, 1988.
- Gorshkov, S. G. (Ed.), *World Ocean Atlas, vol. 3, Arctic Ocean* (in Russian), 189 pp., Pergamon, New York, 1983.
- Gregg, M. C., Diapycnal mixing in the thermocline—A review, *J. Geophys. Res.*, 92, 5249–5286, 1987.
- Gregg, M. C., Scaling turbulent dissipation in the thermocline, *J. Geophys. Res.*, 94, 9686–9698, 1989.
- Guest, P. S., and K. L. Davidson, The effect of observed ice conditions on the drag coefficient in the summer East Greenland Sea marginal ice zone., *J. Geophys. Res.*, 92, 6943–6954, 1987.
- Haidvogel, D. B., and T. Keffer, Tracer dispersal by mid-ocean mesoscale eddies, Pt. I,

- Ensemble statistics, *Dyn. Atmos. Oceans*, 8, 1-40, 1984.
- Häkkinen, S., and D. J. Cavalieri, A study of oceanic surface heat fluxes in the Greenland, Norwegian, and Barents seas, *J. Geophys. Res.*, 94, 6145-6157, 1989.
- Hanzlick, D. J., The West Spitzbergen Current: Transport, forcing, and variability, Ph.D. thesis, 127 pp., Univ. of Wash., Seattle, 1983.
- Hopkins, T. S., The GIN Sea, *Earth-Science Reviews*, 30, 175-318, 1991.
- Huang, N. E., An estimate of the influence of breaking waves on the dynamics of the upper ocean, in *Wave Dynamics and Radio Probing of the Ocean Surface*, pp. 295-314, edited by O. M. Phillips and K. Hasselmann, Plenum, New York, 1986.
- Johannessen, J. A., O. M. Johannessen, E. Svendsen, et al., Mesoscale eddies in the Fram Strait marginal ice zone during the 1983 and 1984 Marginal Ice Zone Experiments, *J. Geophys. Res.*, 92, 6754-6772, 1987.
- Jones, D. W., Velocity profiler (XCP) observations of a bottom boundary layer in the Strait of Juan de Fuca, *APL-UW TR 8927*, Appl. Phys. Lab., Univ. of Wash., Seattle, 1989.
- Josberger, E. G., Sea ice melting in the marginal ice zone, *J. Geophys. Res.*, 88, 2841-2844, 1983.
- Kraus, E. B., and J. S. Turner, A one-dimensional model of the seasonal thermocline, II, The general theory and its consequences, *Tellus*, 19, 98-106, 1967.
- Lueck, R. G., Thermal inertia of conductivity cells: Theory, *J. Atmos. Oceanic Technol.*, 7, 741-755, 1990.

- Lueck, R. G., and J. J. Picklo, Thermal inertia of conductivity cells: Observations with a Sea-Bird cell, *J. Atmos. Oceanic Technol.*, 7, 756–768, 1990.
- Manley, T. O., R. H. Bourke, and K. L. Hunkins, Near-surface circulation over the Yermak Plateau in northern Fram Strait, *J. Mar. Systems*, 3, 107–125, 1992.
- Maykut, G. A., An introduction to ice in the polar oceans, *Tech. Rep. APL-UW 8510*, Appl. Phys. Lab., Univ. of Wash., Seattle, 1985.
- McPhee, M. G., The upper ocean, in *Geophysics of Sea Ice*, edited by N. Untersteiner, pp. 339–394, Plenum, New York, 1986.
- McPhee, M. G., A time-dependent model for turbulent transfer in a stratified oceanic boundary layer, *J. Geophys. Res.*, 92, 6977–6986, 1987.
- Moore, R. M., and D. W. R. Wallace, A relationship between heat transfer to sea ice and the temperature-salinity properties of Arctic ocean waters, *J. Geophys. Res.*, 93, 565–571, 1988.
- Morison, J. H., J. G. McPhee, and G. A. Maykut, Boundary layer, upper ocean, and ice observations in the Greenland Sea marginal ice zone, *J. Geophys. Res.*, 92, 6987–7011, 1987.
- Morison, J. H., R. H. Andersen, N. G. Larson, E. A. D'Asaro, and T. Boyd, The correction for thermal inertia effects in Sea-Bird CTD data, submitted to *J. Atmos. Oceanic Technol.*, 1993.
- Muench, R. D., M. G. McPhee, C. A. Paulson, and J. H. Morison, Winter oceanographic conditions in the Fram Strait-Yermak Plateau region, *J. Geophys. Res.*, 97, 3469–3483

1992.

Niiler, P. P., One-dimensional models of the seasonal thermocline, in *The Sea, Ideas and Observations on Progress in the Study of the Sea*, pp. 97–115, vol. VI, edited by E. D. Goldberg et al., Wiley, New York, 1977.

Oakey, N. S., and J. A. Elliott, Dissipation within the surface mixed layer, *J. Phys. Oceanogr.*, *12*, 171–185, 1982.

Padman, L., and T. M. Dillon, Turbulent mixing near the Yermak Plateau during the Coordinated Eastern Arctic Experiment, *J. Geophys. Res.*, *96*, 4769–4782, 1991.

Padman, L., A. J. Plueddemann, R. D. Muench, and R. T. Pinkel, Diurnal tides near the Yermak Plateau, *J. Geophys. Res.*, *97*, 12,639–12,652, 1992.

Pease, C. H., The size of wind-driven coastal polynyas, *J. Geophys. Res.*, *92*, 7049–7059, 1987.

Perkin, R. G., and E. L. Lewis, Mixing in the West Spitzbergen Current, *J. Phys. Oceanogr.*, *14*, 1315–1325, 1984.

Quadfasel, D., and J. Meincke, Note on the thermal structure of the Greenland Sea gyres, *Deep Sea Res.*, *34*, 11A, 1883, 1987.

Sanford, T. B., Recent improvements in ocean current measurement from motional electric fields and currents, in *Proc. IEEE Third Working Conf. on Current Measurement*, Airlie, Virginia, 1986.

Sanford, T. B., R. G. Drever, J. H. Dunlap, and E. A. D'Asaro, Design, operation, and performance of an expendable temperature and velocity profiler (XTVP), *APL-UW 8110*,

- Appl. Phys. Lab., Univ. of Wash., Seattle, 1982.
- Stull, R. B., *An Introduction to Boundary Layer Meteorology*, Kluwer, Boston, 1988.
- Swift, J. H., and K. Aagaard, Seasonal transitions and water mass formation in the Iceland and Greenland Seas, *Deep Sea Res.*, 28, 10A, 1107–1129, 1981.
- Turner, J. S., *Buoyancy Effects in Fluids*, 367 pp., Cambridge University Press, New York, 1973.
- Untersteiner, N., On the ice and heat balance in Fram Strait, *J. Geophys. Res.*, 93, 527–531, 1988.
- Vinje, T., Drift, composition, morphology and distribution of the sea ice fields in the Barents Sea—long term observations, *Skr. Nor. Polarinst.*, 179C, 1985.
- Wijesekera, H., L. Padman, T. Dillon, M. Levine, C. Paulson, and R. Pinkel, The application of internal-wave dissipation models to a region of strong mixing, *J. Phys. Oceanogr.*, 23, 269–286, 1992.
- Worthington, L. V., The Norwegian Sea as a Mediterranean basin, *Deep Sea Res.*, 17, 77–84, 1970.
- Wu, J., Wind induced turbulent entrainment across a stable density interface, *J. Fluid Mech.*, 61, 275–287, 1973.

FIGURES

Fig. 1. Map of operating area. Measurements were made along a nearly straight section of the continental shelf and slope west of Spitzbergen.

Fig. 2. Example of CTD processing. Dashed profile is uncorrected data. Solid profile is data with thermal lag correction applied. The correction removes density inversions associated with rapid temperature changes (1 MPa = 100 dbars).

Fig. 3. Map of potential temperature at 150 m depth from all CTD data. Colored symbols show the location of data points; the color indicates the temperature as given on the scale. Colored contours display an objective mapping of the temperature. Temperatures greater than 4°C are shaded red. The warm core of the West Spitzbergen Current is apparent.

Fig. 4. Potential temperature and density sections. Colored symbols show the location of data points; the color indicates the temperature as given on the scale. Colored contours display an objective mapping of the temperature. Temperatures greater than 4°C are shaded red. The temperature contour interval is 0.2°C. Dark contours indicate the same objective mapping of σ_θ . The density contour interval is 0.05 kg m⁻³. First section (a) is at Bjornoya. The data locations for Figures 4b–4e are shown in Figure 3, and the approximate downstream location is given on each map. The warm core of the West Spitzbergen Current is apparent over the slope in each section.

Fig. 5. Near-surface velocity vectors computed from ship's speed log and gyrocompass heading and GPS navigation. Careful editing has resulted in this small set of vectors. Geographical regions defined by the depth contours and the dotted lines are labeled. The water flows northward along the slope.

Fig. 6. Average downstream and onshore surface velocity in each of the regions defined in Figure 5. Error bars are one standard deviation.

Fig. 7. Section of downstream velocity from XCP data. Contour interval is 0.1 m s^{-1} . The maximum surface velocity is just above 0.5 m s^{-1} . Heavier shading indicates northward flow. Velocity offsets for each XCP profile have been estimated (see text) and the data objectively mapped for plotting here. Note much larger depth axis than in other sections.

Fig. 8. Streamtube locations in each section. The cross section of each of the three streamtubes is superimposed on the temperature contours from each section. The largest is streamtube 1; the smallest, streamtube 2; and the one with constant shape, streamtube 3.

Fig. 9. Average temperature (*a*) and salinity (*b*) in each streamtube computed from objectively mapped fields. Errors are one standard deviation of the mean. Solid line is fit of streamtube 1. Table 2 gives other fits. Temperature decreases uniformly to the north. Salinity varies irregularly.

Fig. 10. Ice concentration from SSM/I for (a) day 17 and (b) day 31. The box defines our approximate operating area and the region of heat flux calculations in Figure 12. Note that the ice cover in this region has increased with time.

Fig. 11. Ice concentration from SSM/I as a function of time and cross-stream distance at (a) $y = 50$ km and (b) $y = -50$ km. Note that the ice cover increases with time, first in the south and then in the north.

Fig. 12. Heat flux from the ocean to the ice. (a) Measured wind speed (solid curve) and resulting ice speed (dashed). (b) Wind and ice directions. (c) Average ice concentration in box (solid) and along the cardinal edges of the box (dashes and dots as labeled). (d) Heat flux to ice from ice melt model (solid) and from ice divergence model with an assumed ice thickness of 0.33 m (dashed). The heat flux to the ice increases as the ice concentration increases.

Fig. 13. Heat flux to the ice and atmosphere. (a) Wind speed. (b) Air temperature and water temperature. (c) Sensible and latent heat fluxes, $Q_s + Q_e$ (bottom line); total atmospheric heat flux Q (middle line); atmospheric and ice heat fluxes, $Q + H$ (top).

Fig. 14. Temperature-salinity diagrams corresponding to each section in Figure 4. Actual data points, not objectively analyzed data, are plotted. Symbol denotes geographic location of data as marked in Figure 4: 'O' for warm core defined by stream-tube 1, '*' for slope data outside of warm core, 'x' for Greenland Sea, and '+' for shelf. Dotted lines denote densities of 27, 27.5, and 28 kg m^{-3} . Boxes are water mass

categories defined by *Aagaard et al.* [1985] and abbreviated Arctic Surface Water (ASW), Polar Water (PW), Polar Intermediate Water (PIW), Deep Water (DW), Upper Arctic Intermediate Water (UAIW), Lower Arctic Intermediate Water (LAIW), and Atlantic Water (AW). The line labeled $Q = 0$ indicates the trajectory of a water parcel cooled by contact with ice. The line labeled $Q = H$ indicates the mixing line of a water parcel cooled an equal amount by ice and the atmosphere.

Fig. 15. Salinity structure for each section in Figure 4. Salinity contours with interval 0.1 psu are shaded. Water saltier than 34.85 psu has the lightest shading; this corresponds to the salinity of the incoming Atlantic Water. Density is contoured as in Figure 4. Mixed layer depths are indicated by the white symbols.

Fig. 16. Successive temperature profiles from tow-yo CTD profiling through the edge of the warm core near $y = 0$ km. The entire sequence is only about 6 km long. Note the extreme variability in this short distance.

Fig. 17. Mixed layer depths from all CTD profiles plotted against across-stream distance. Triangles indicate no mixed layer; squares indicate a mixed layer deeper than the profile. Notice very shallow and variable mixed layers over the warm core.

Fig. 18. Conceptual stages in the cooling of the warm core of the West Spitzbergen Current. I. Cold air directly cools the warm core producing cold, salty water. II. Ice advects over the warm core and melts, directly cooling and freshening it. Cold air continues to cool the warm core though leads. Cold, but fresher water is produced. III.

Cold fresh water covers warm core. Cooling continues, however, via mixing along the isopycnals which connect the warm core to the surface. The ice edge intermittently advects over this outcropping, so that both cold salty water and cold fresh water are produced.